



Finite element simulations of dynamics of multivariant martensitic phase transitions based on Ginzburg–Landau theory

J.-Y. Cho^{a,b,c}, A.V. Idesman^{c,*}, V.I. Levitas^d, T. Park^a

^a Hanyang University, Department of Civil and Environmental Engineering, Seoul, Republic of Korea

^b Louisiana State University, Department of Civil and Environmental Engineering, Baton Rouge, Louisiana 70803-6405, USA

^c Texas Tech University, Department of Mechanical Engineering, Lubbock, TX 79409-1021, USA

^d Iowa State University, Departments of Aerospace Engineering, Mechanical Engineering, and Material Science and Engineering, Ames, Iowa 50011, USA

ARTICLE INFO

Article history:

Received 6 February 2012

Received in revised form 4 April 2012

Available online 26 April 2012

Keywords:

Martensitic phase transitions

Finite elements

Phase-field approach

Microstructure

ABSTRACT

A finite element approach is suggested for the modeling of multivariant stress-induced martensitic phase transitions (PTs) in elastic materials at the nanoscale for the 2-D and 3-D cases, for quasi-static and dynamic formulations. The approach is based on the phase-field theory, which includes the Ginzburg–Landau equations with an advanced thermodynamic potential that captures the main features of macroscopic stress–strain curves. The model consists of a coupled system of the Ginzburg–Landau equations and the static or dynamic elasticity equations, and it describes evolution of distributions of austenite and different martensitic variants in terms of corresponding order parameters. The suggested explicit finite element algorithm allows decoupling of the Ginzburg–Landau and elasticity equations for small time increments. Based on the developed phase-field approach, the simulation of the microstructure evolution for cubic-tetragonal martensitic PT in a NiAl alloy is presented for quasi-static (i.e., without inertial forces) and dynamic formulations in the 2-D and 3-D cases. The numerical results show the significant influence of inertial effects on microstructure evolution in single- and polycrystalline samples, even for the traditional problem of relaxation of initial perturbations to stationary microstructure.

© 2012 Elsevier Ltd. All rights reserved.

1. Introduction

The models based on phase-field or Ginzburg–Landau theory can describe the complicated martensitic microstructure consisting of austenite and martensitic variants in terms of distribution of the order parameters. In the Ginzburg–Landau theory, free energy is the function of order parameters, and the field equations are derived from the application of thermodynamic laws. The known approaches based on Ginzburg–Landau theory for the modeling of martensitic phase transformation in elastic materials (see Wang and Khachaturyan, 1997; Artemev et al., 2000, 2001; Seol et al., 2002, 2003; Ichitsubo et al., 2000; Saxena et al., 1997; Shenoy et al., 1999; Rasmussen et al., 2001; Ahluwalia et al., 2003; Lookman et al., 2003a,b; Jacobs, 2000; Curnoe and Jacobs, 2001a,b; Jacobs et al., 2003) differ in their choice of:

- the order parameters (selected strain components or transformation strain-related variables) that describe the evolution of each martensitic variant;
- thermodynamic potentials;
- the total number of equations (additional kinetic equations for the order parameters are introduced if the order parameters are the transformation strain-related variables);
- elasto-static or elasto-dynamic formulations; and,
- numerical algorithms.

In Wang and Khachaturyan (1997), Artemev et al. (2000, 2001) and Seol et al. (2002, 2003), the free energy is expressed in terms of transformation strain-related order parameters. Field equations for the determination of strains are derived using the minimization of the free energy with respect to strains, which leads to elasto-static equations; field equations for the order parameters are formulated as evolution equations based on the time-dependent Ginzburg–Landau kinetic equations. The time-dependent Ginzburg–Landau equations include the driving forces for the change of the order parameters. The driving forces are derived as the corresponding variational derivatives of the free energy.

* Corresponding author. Tel.: +1 (806) 742 3563; fax: +1 (806) 742 3540.

E-mail address: alexander.idesman@coe.ttu.edu (A.V. Idesman).

The elasto-static equations in Wang and Khachaturyan (1997), Artemev et al. (2000, 2001) and Seol et al. (2002, 2003) are solved analytically using the Fourier transform, and the time-dependent Ginzburg–Landau kinetic equations with the periodic boundary conditions are solved numerically using a spectral method. Thus, to our best knowledge, all solutions for the models with the transformation strain-related order parameters were based on the static formulations; i.e., on the mechanical equilibrium equations.

In Curnoe and Jacobs (2001a,b), Jacobs et al. (2003) and Lookman et al. (2003a,b), the order parameters are some components of the strain tensor, and the free energy depends on them and their gradients. The field equations are derived from the minimization of the free energy for statics or using the Lagrangian formulation for dynamics, which includes inertial forces. Also, dissipative stresses based on a Rayleigh dissipative function are introduced for the dynamics formulation in order to obtain a stationary solution. The time-dependent Ginzburg–Landau equations are not used for the formulation of the field equations. It is necessary to note that if the strain gradients would be dropped from the free energy, then these formulations reduce to standard non-linear elasticity equations for statics or standard non-linear viscoelastic equations (due to the Rayleigh dissipative function) for dynamics. The inclusion of the strain gradients yields non-local constitutive relationships between stresses and strains (i.e., stresses depend on strains and strain gradients). The modeling of phase transitions in the 2-D case considered in Curnoe and Jacobs (2001a,b) and Jacobs et al. (2003) did not include the inertial forces; i.e., a quasi-static formulation (the equilibrium equations) for viscoelastic materials was actually used instead of dynamics. In contrast, (Lookman et al., 2003a,b) presented the detailed analytical and numerical studies of phase transformations with inertial forces (i.e., using the complete dynamic formulation) for the 2-D formulation. While the dynamic equation of motion is the same in all papers (because it is independent of the constitutive equations), Lookman et al. (2003a,b) presented the final equations in terms of the strain tensor with a constraint due to St. Venant's strain compatibility conditions. Along with numerical examples, this allowed them to perform an analytical study in the 2-D case for various phase transformations. However, in the 3-D case, the strain-based formulation has six unknown components of the strain tensor and three differential strain compatibility constraints. At the same time, the displacement-based formulation has just three unknown displacements. Detailed 1-D study of the dynamics of phase transformations was performed in Truskinovsky and Vainchtein (2008, 2006), Truskinovsky (1994a,b) and Theil and Levitas (2000).

Levitas and Preston (2002a,b) and Levitas et al. (2003) developed advanced thermodynamic potentials based on the transformation strain-related order parameters that, in contrast to the aforementioned approaches, can describe the typical stress–strain curves observed experimentally, and that include all of the temperature-dependent thermomechanical properties of austenite and martensitic variants. They describe phase transformations between austenite and martensitic variants and between martensitic variants with arbitrary types of symmetry. We were unable to obtain the same results when the total strain-related order parameters (like in Curnoe and Jacobs (2001a,b), Jacobs et al. (2003) and Lookman et al. (2003a,b)) are used. That is why all our further developments (including the current paper) were focused on the transformation strain-related order parameters. Large-strain extension of this theory and corresponding simulations are presented in Levitas et al. (2009). The athermal (threshold-type) resistance to interface motion is introduced in Levitas and Lee (2007) and Levitas

et al. (2010), which allowed one to obtain multiphase stationary solutions.

The interface tension and the more sophisticated expression for the gradient energy are introduced in Levitas and Javanbakht (2010, 2011a). The surface-induced barrierless pre-transformations and transformations caused by the reduction in the surface energy during transformation, as well as the scale effect, are described in Levitas et al. (2006), Levitas and Javanbakht (2010) and Levitas and Samani (2011a,b). The finite-width surface layer and the multiple scale and stress effects in surface-induced nucleation were treated in Levitas and Javanbakht (2011b). A microscale version of the theory was presented in Idesman et al. (2005) and Levitas et al. (2004). The 2-D finite element simulations with the static equilibrium equations have been performed in Levitas and Lee (2007), Levitas et al. (2010) and Levitas and Javanbakht (2010, 2011a,b).

In this paper, a numerical approach based on the phase-field theory for the martensitic phase transformation of Levitas and Preston (2002a,b) and Levitas et al. (2003) is expanded for the following cases:

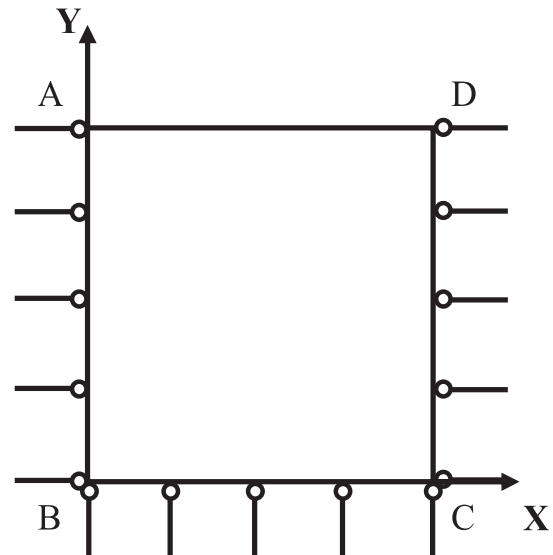


Fig. 1. Cross-section of the plate.

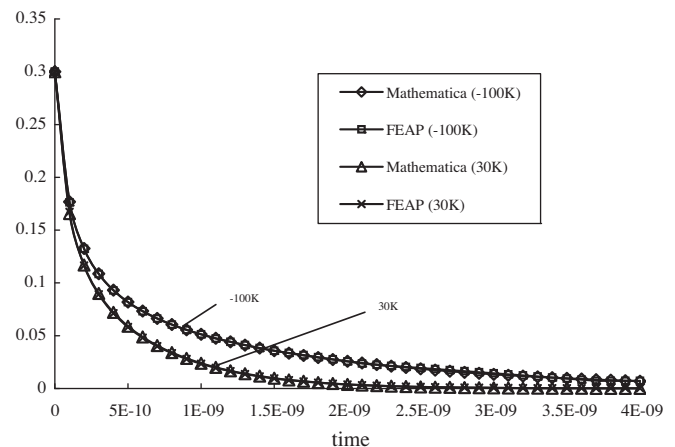


Fig. 2. Time variation of the order parameter η for test problem.

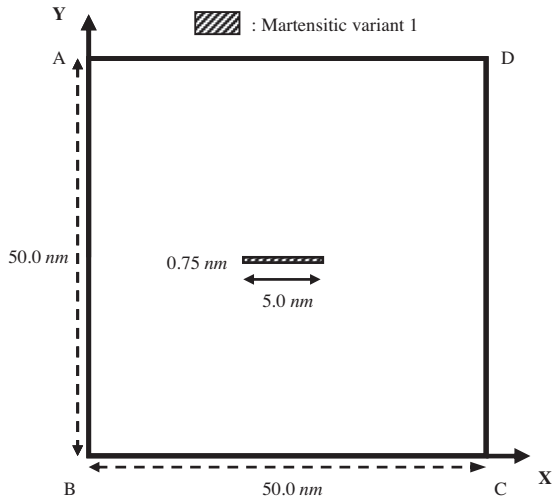


Fig. 3. An austenitic plate with a thin martensitic nucleus ($\eta_1 = 1$) at the center.

- (a) The elasto-dynamics equations (with inertial forces) are used, which has not been done before for theories based on transformation strain-related order parameters (see Section 2). Characteristic time of occurring of phase transformation in the material point is of the order of magnitude of 1 ps. Since transformation strain of the order of magnitude of 0.1 should be introduced during such a short time, material inertia is expected to play an important part even when there is no dynamic mechanical loading.
- (b) A new finite element approach to the solution of the coupled elasto-dynamics and time-dependent Ginzburg–Landau equations is developed (see Section 3). Since the time-dependent Ginzburg–Landau equations for n order parameters are similar to the heat transfer equation, the total system of equations for the modeling of phase transformation is similar to the system of coupled thermoelasticity and heat transfer equations with n temperatures. Despite the fact that the finite element method is a very popular tool for the solution of elasticity and heat transfer equations, we have not seen in the literature the applica-

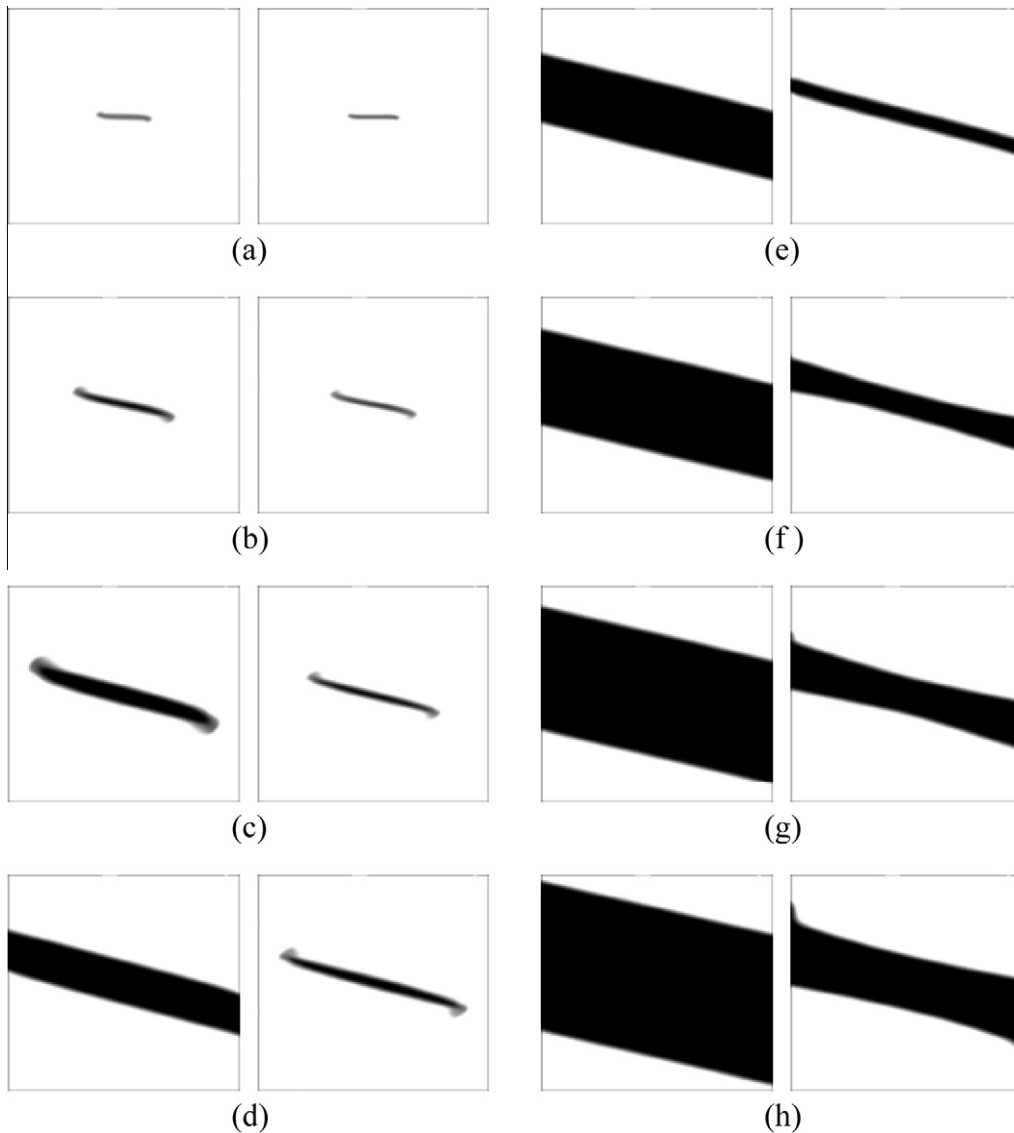


Fig. 4. Growth patterns for the thin nucleus. (a)–(h) show the distribution of the order parameter in the static (left) and dynamic (right) cases at time 0.3 ps, 3.0 ps, 6.0 ps, 9.0 ps, 12 ps, 15 ps, 18 ps, and 21 ps, respectively.

tion of the finite element method to the solution of the dynamic phase-field and elasticity equations for martensitic phase transitions.

- (c) Microstructure evolution in 2-D polycrystalline sample is studied in static and dynamic formulations (see Section 4).
- (d) Microstructure evolution in 3-D formulation in a single crystal is studied in static and dynamic formulations (see Section 4.4).

Thus, in comparison with the known models with transformation strain-related order parameters (Wang and Khachaturyan, 1997; Artemev et al., 2000, 2001; Seol et al., 2002, 2003), a more advanced potential and the dynamic formulation have been used. In contrast to the known simulations with the dynamic models based

on the strain-related order parameters (Lookman et al., 2003a,b), the 3-D solutions for a single and polycrystalline sample are presented for the completely different constitutive formulation.

The paper has the following structure. The system of equations for the phase-field approach for the martensitic phase transformation at nano-scale is described in Section 2. The coupled system of equations includes the elasto-dynamics equations and the time-dependent Ginzburg–Landau equations. The advanced thermodynamic potential developed in Levitas and Preston (2002a,b) is used in this study. In Section 3, a finite element algorithm for the solution of the system of equations is suggested. Because the time-dependent Ginzburg–Landau equations for the order parameters are similar to the heat transfer equations, the total system of equations for the modeling of phase transitions is similar to the system of coupled thermoelasticity and heat

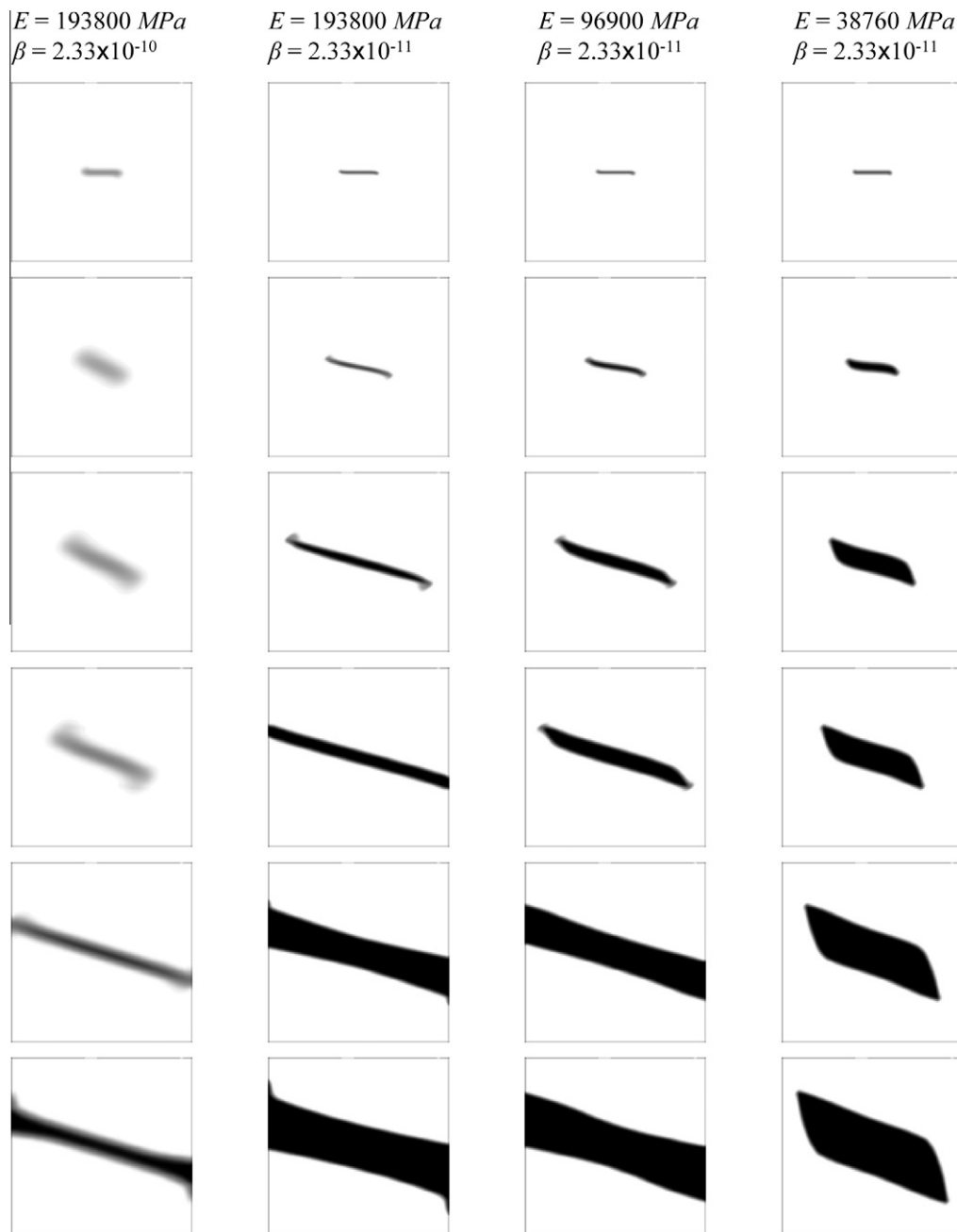


Fig. 5. Evolution of a martensitic nucleus (the order parameter η) in a dynamic problem for the different values of Young's modulus E and parameter β at time 0.3 ps, 3.0 ps, 9.0 ps, 12 ps, 18 ps, and 21 ps (from the top to the bottom).

transfer equations. The modeling of multi-variant martensitic phase transformation in 2-D and 3-D single-crystal and poly-crystal specimens is considered in Section 4. The morphology and evolution of the microstructure during martensitic phase transformation are modeled and compared for the cases of statics and dynamics formulations. The effects of elastic properties, gradient energy, crystal orientation, and polycrystalline structure are elucidated for 2-D and 3-D formulations. Some preliminary results have been presented in our short letter, (Idesman et al., 2008).

Contractions of tensors $\mathbf{A} = \{A_{ij}\}$ and $\mathbf{B} = \{B_{ji}\}$ over one and two indices are designated as $\mathbf{A} \cdot \mathbf{B} = \{A_{ij} B_{jk}\}$ and $\mathbf{A} : \mathbf{B} = A_{ij} B_{ji}$, correspondingly, and ∇ is the gradient operator.

2. Phase-field model for multivariant martensitic phase transformations

Multi-variant martensitic microstructure may consist of austenite and n symmetry-related martensitic variants and can be represented in terms of the distribution of n order parameters η_k ($k = 1, 2, \dots, n$). Transformation strain $\boldsymbol{\varepsilon}_{tk}$ transforms crystal lattice of austenite into crystal lattice of k th martensitic variant. A list of transformation strains for transformation to different types of crystal lattices is available (e.g., in Bhattacharya (2003)). The order parameters η_k vary from zero to unity, where $\eta_k = 1$ corresponds to the k th martensitic variant, $\eta_k = 0$ corresponds to austenite or other martensitic variants, and $0 < \eta_k < 1$ represents transitional regions or interfaces. For simplicity, the constant temperature is considered; however, the technique can be easily extended to a non-isothermal case. In Ginzburg–Landau theory for martensitic phase transitions the Helmholtz free-energy density $\psi(\boldsymbol{\varepsilon}, \eta_i, \eta_{i,j}, \theta)$ is assumed to be a function of the strain components $\boldsymbol{\varepsilon}$, the order parameters η_i and the gradients of the order parameters $\eta_{i,j}$, as well as the temperature θ . The Helmholtz free energy $\bar{\psi}$ can be expressed as

$$\bar{\psi} = \int_D \psi(\boldsymbol{\varepsilon}, \eta_i, \eta_{i,j}, \theta) dV, \quad (1)$$

where D is the volume. For the order parameters η_k , the time-dependent Ginzburg–Landau kinetic equations have the form

$$\frac{\partial \eta_k}{\partial t} = - \sum_{p=1}^n L_{kp} \frac{\delta \bar{\psi}}{\delta \eta_p} \Big|_{\boldsymbol{\varepsilon}} + \zeta_k, \quad k = 1, 2, \dots, n, \quad (2)$$

where L_{kp} are positive definite kinetic coefficients, $\delta \bar{\psi} / \delta \eta_p$ is the variational derivative that determines the local thermodynamic driving force for transformation, and ζ_k is the noise due to thermal fluctuations that satisfies the dissipation-fluctuation theorem; see (Wang and Khachaturyan, 1997; Artemev et al., 2000, 2001). The variational derivative in Eq. (2) is evaluated at constant $\boldsymbol{\varepsilon}$. After some simplifications, the total system of equations is presented in Box 1.

Box 1. Problem formulation.

1. Kinematics

Decomposition of the strain tensor $\boldsymbol{\varepsilon}$

$$\boldsymbol{\varepsilon} = 0.5(\nabla \mathbf{u} + \nabla \mathbf{u}^T); \quad \boldsymbol{\varepsilon} = \boldsymbol{\varepsilon}_e + \boldsymbol{\varepsilon}_t. \quad (3)$$

Transformation strain $\boldsymbol{\varepsilon}_t$

$$\begin{aligned} \boldsymbol{\varepsilon}_t &= \sum_{k=1}^n \boldsymbol{\varepsilon}_{tk} \varphi(\eta_k) - \sum_{i=1}^{n-1} \sum_{j=i+1}^n \eta_i^2 \eta_j^2 (\eta_i \mathbf{L}_{ij} + \eta_j \mathbf{L}_{ji}); \\ \mathbf{L}_{ji} &= (a-3)\boldsymbol{\varepsilon}_{ti} + 3\boldsymbol{\varepsilon}_{tj}; \quad \varphi(\eta_i) = a\eta_k^2(1-\eta_k)^2 \\ &\quad + (4\eta_k^3 - 3\eta_k^4). \end{aligned} \quad (4)$$

2. Helmholtz free energy and its contributions

$$\psi = \psi^e(\boldsymbol{\varepsilon}, \eta_i, \theta) + \psi^\theta + \psi^\nabla. \quad (5)$$

2.1. Elastic energy for equal elastic properties of phases

$$\psi^e = 0.5\boldsymbol{\varepsilon}_e : \mathbf{C} : \boldsymbol{\varepsilon}_e = 0.5(\boldsymbol{\varepsilon} - \boldsymbol{\varepsilon}_t) : \mathbf{C} : (\boldsymbol{\varepsilon} - \boldsymbol{\varepsilon}_t). \quad (6)$$

2.2. The thermal part of the Helmholtz free energy

$$\psi^\theta = \sum_{k=1}^n f(\theta, \eta_k) + \sum_{i=1}^{n-1} \sum_{j=i+1}^n F_{ij}(\eta_i, \eta_j) \quad (7)$$

with

$$f(\eta_k) = A\eta_k^2 + (4\Delta G^\theta - 2A)\eta_k^3 + (A - 3\Delta G^\theta)\eta_k^4; \quad (8)$$

$$\begin{aligned} F_{ij}(\eta_i, \eta_j) &= \eta_i \eta_j (1 - \eta_i - \eta_j) \{ B[(\eta_i - \eta_j)^2 - \eta_i - \eta_j] \\ &\quad + D\eta_i \eta_j \} + \eta_i^2 \eta_j^2 (\eta_i + \eta_j)(\bar{A} - A); \end{aligned} \quad (9)$$

$$\Delta G^\theta = A_0(\theta - \theta_e)/3; \quad A = A_0(\theta - \theta_e). \quad (10)$$

2.3. Gradient energy

$$\psi^\nabla = \frac{\beta}{2} \sum_{i=1}^n |\nabla \eta_i|^2. \quad (11)$$

3. Hooke's law

$$\boldsymbol{\sigma} = \frac{\partial \psi^e}{\partial \boldsymbol{\varepsilon}} = \mathbf{C} : \boldsymbol{\varepsilon}_e. \quad (12)$$

4. Ginzburg–Landau equations

$$\begin{aligned} \frac{1}{L} \frac{\partial \eta_i}{\partial t} &= \boldsymbol{\sigma} : \frac{\partial \boldsymbol{\varepsilon}_t}{\partial \eta_i} - \frac{\partial \psi^\theta}{\partial \eta_i} + \beta \left(\frac{\partial^2 \eta_i}{\partial x_1^2} + \frac{\partial^2 \eta_i}{\partial x_2^2} + \frac{\partial^2 \eta_i}{\partial x_3^2} \right), \\ i &= 1, \dots, n. \end{aligned}$$

5. Equation of motion

$$\nabla \cdot \boldsymbol{\sigma} = \rho \ddot{\mathbf{u}}. \quad (14)$$

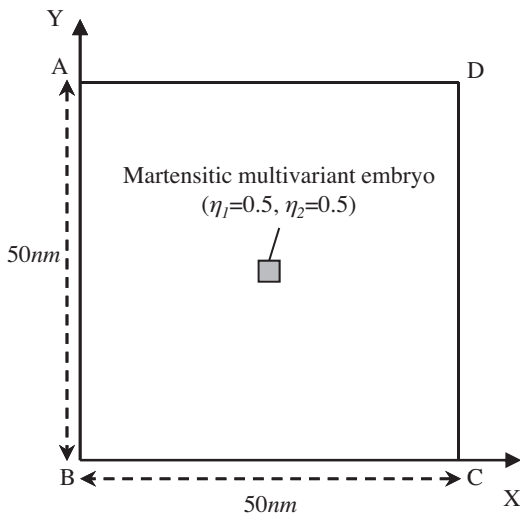


Fig. 6. A 2-D square austenitic specimen with an initial martensitic multivariant embryo.

Here, θ_e and θ_c are the equilibrium temperature and temperature of the loss of stability of the austenite; $a, A_0, \bar{A}, \beta, B, D, L$ are material parameters; \mathbf{C} is the elasticity tensor; and ρ is the mass density. As the simplest case, we accepted $L_{mn} = L\delta_{mn}$, where δ_{mn} is the Kronecker delta.

Eq. (3) represents the standard kinematical equations expressing strains in terms of displacements, as well as additive decomposition of the total strain into elastic and transformational parts. The explicit expressions for transformation strain and for the Helmholtz free energy, Eqs. 4–11, are justified in Levitas and Preston (2002a,b), Levitas et al. (2003, 2009), and Levitas and Javanbakht (2010). Hooke's law is presented by Eq. (12). The substitution of the expressions 5–11 for the Helmholtz energy in the Ginzburg–Landau Eq. (2) results in Eq. (13) ($\zeta_k = 0$ is assumed). Finally, the standard

equations of motion are presented by Eq. (14). Eqs. (3)–(14) with corresponding boundary and initial conditions form a system of partial differential equations for the modeling of martensitic phase transitions - i.e. for the determination of order parameters η_k , displacements \mathbf{u} , strains $\boldsymbol{\varepsilon}$, and stresses $\boldsymbol{\sigma}$.

Let us analyze a system of Eqs. 3–14. Eqs. (3), (12) and (14) represent the standard thermoelastodynamics equations with the transformation strain $\boldsymbol{\varepsilon}_t$ that can be treated as the thermal strain for a numerical solution. Eq. (13) is similar to the standard non-stationary heat transfer equation for the temperature θ

$$\rho c \frac{\partial \theta}{\partial t} = k \left(\frac{\partial^2 \theta}{\partial x_1^2} + \frac{\partial^2 \theta}{\partial x_2^2} + \frac{\partial^2 \theta}{\partial x_3^2} \right) + Q. \quad (15)$$

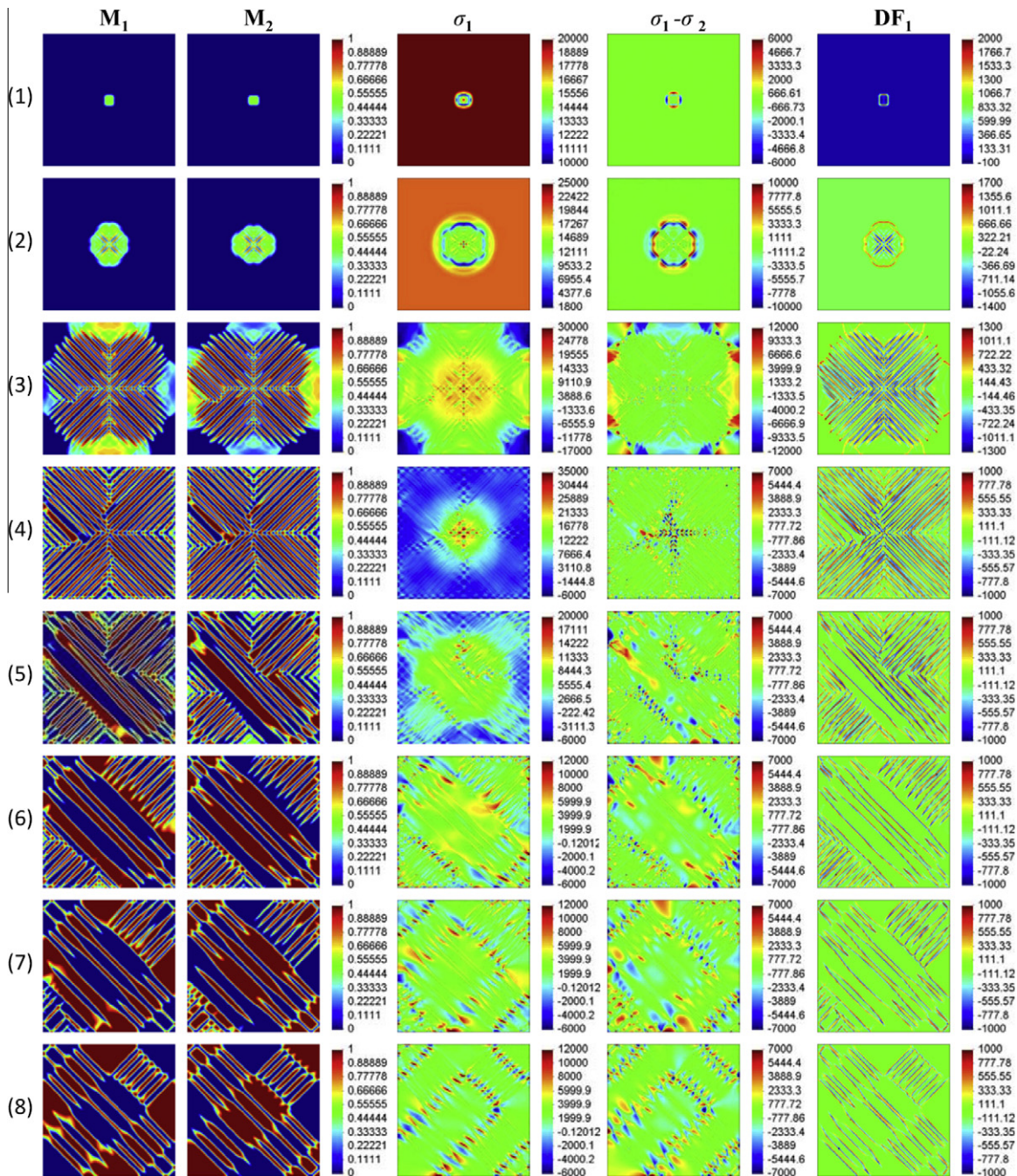


Fig. 7. Evolution of the martensitic embryo at the center of the specimen in the dynamic case. The first, second, third, fourth, and fifth columns correspond to $\eta_1, \eta_2, \sigma_1, \sigma_1 - \sigma_2$, and $\partial G / \partial \eta_1$ (the local driving force for the evolution of η_1), respectively. Rows (1)–(8) correspond to times 0.3 ps, 1.5 ps, 6.0 ps, 15 ps, 27 ps, 42 ps, 60 ps, and 420 ps, respectively.

If $i = n = 1$ in Eq. (13), we have the standard coupled system of the heat transfer and the elastodynamics equations. If $n > 1$, we have the coupled system of the n heat transfer equations and the elastodynamics equations. Coupling follows from the facts that the transformation strain ϵ_t in the elastodynamics equations depends on the order parameters η_k and that the term $\sigma : \frac{d\epsilon_t}{dt}$ in Eq. (13) depends on the stress tensor.

Isotropic elasticity with equal elastic properties of phases is used for simplicity. The following material parameters for cubic to tetragonal phase transformation in NiAl alloy are used for all problems considered below (see Levitas and Preston, 2002a,b; Levitas et al., 2003, 2010), unless otherwise stated: $a = 2.98$, $A = 5320$ MPa, $\theta_e = 215$ K, $\theta_c = -183$ K, $A_0 = 4.4$ MPa/K, $B = 0$,

$D = 5000$ MPa, $\beta = 2.33 \times 10^{-11}$ N, $L = 2596.5$ m²/Ns, the Young's modulus $E = 198,300$ MPa, the Poisson's ratio $\nu = 0.33$, and $\rho = 5850$ kg/m³. The transformation strains ϵ_{ti} for the martensitic variants \mathbf{M}_1 , \mathbf{M}_2 and \mathbf{M}_3 are determined in Levitas and Preston (2002b)

$$\begin{aligned} \epsilon_{t1} &= \{0.215; -0.078; -0.078; 0; 0; 0\}, \\ \epsilon_{t2} &= \{-0.078; 0.215; -0.078; 0; 0; 0\}, \\ \epsilon_{t3} &= \{-0.078; -0.078; 0.215; 0; 0; 0\}. \end{aligned} \tag{16}$$

We assume that the temperature θ is uniformly distributed through the specimen and does not change during phase transformation (the isothermal case). Note that the negative critical temperature

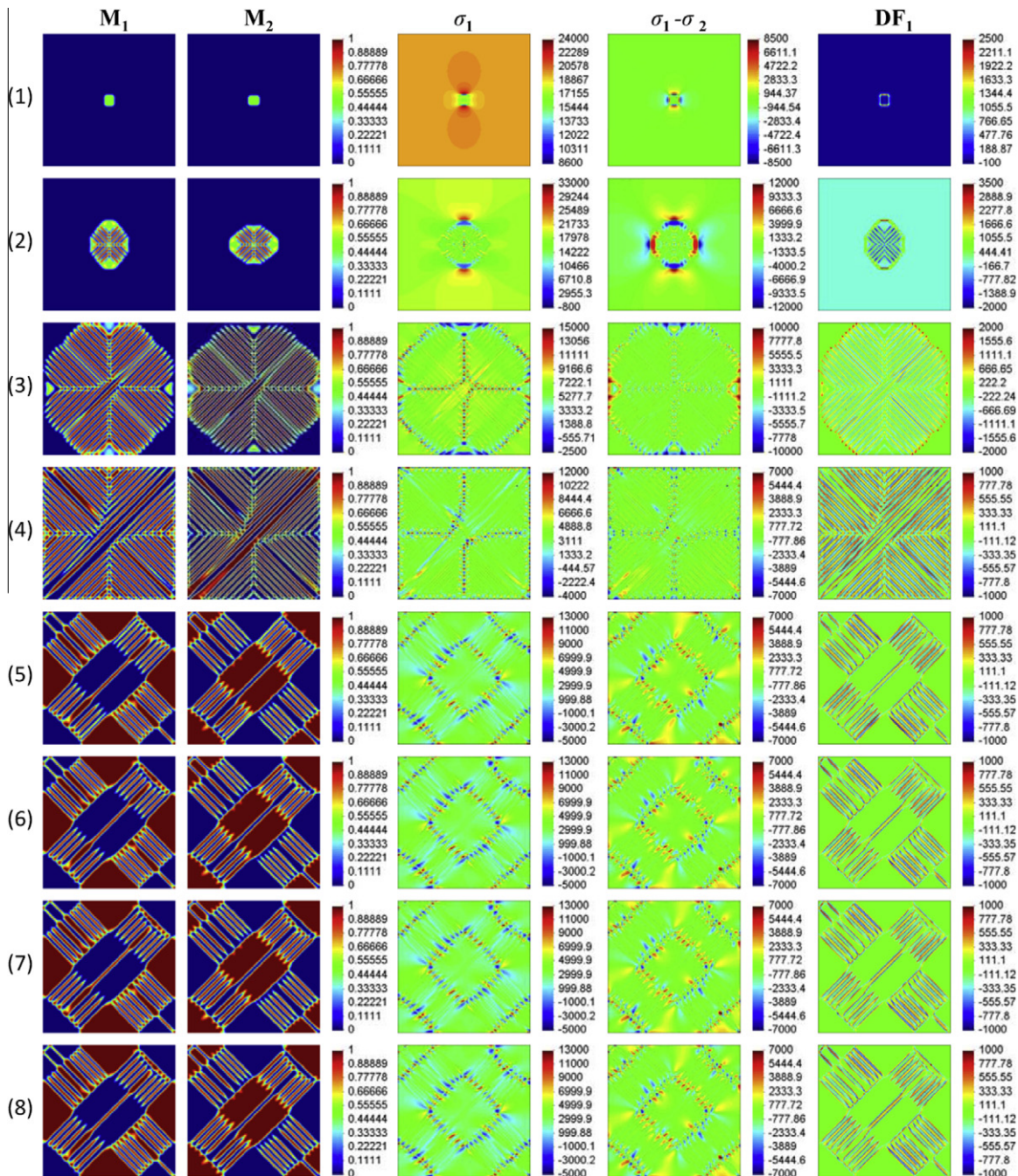


Fig. 8. Evolution of martensitic embryo at the center of the specimen (static solution). Left two columns: η_1 and η_1 ; third and fourth columns: σ_1 and $\sigma_1 - \sigma_2$; right column: $\partial G/\partial \eta_1$, the local driving force for evolution of η_1 . Rows (1)–(8) correspond to times 0.3 ps, 1.5 ps, 6.0 ps, 15 ps, 27 ps, 42 ps, 60 ps, and 420 ps, respectively.

θ_c is the material parameter of the used model. This means that at $\theta_c < 0$ and $\theta > 0$ (the actual temperature θ is always positive), the austenitic phase cannot get unstable at zero stresses; the required stress for the austenite instability at any $\theta > 0$ can be also found from the model used.

The boundary conditions for the i th order parameter for all problems considered in the paper are

$$\mathbf{n} \cdot \nabla \eta_i = 0, \quad i = 1, \dots, n, \quad (17)$$

where \mathbf{n} is the outward unit normal to the boundary.

The mechanical part of the problem will include the following typical boundary conditions: at free boundary

$$\sigma_n = \tau_n = 0, \quad (18)$$

at fixed boundary without friction

$$u_n = \tau_n = 0, \quad (19)$$

where σ_n , τ_n , and u_n are the normal and shear stresses and the normal displacements at the boundary with the normal \mathbf{n} .

3. Finite element algorithm

We will use finite elements for the space discretization of the partial differential Eqs. (3)–(14). Then, for the time integration of the obtained coupled system of finite element equations, we suggest the following step-by-step procedure. The total observation time is divided into N time steps with the small time increments Δt . In order to find unknown quantities at the end of each small time step Δt , we assume that: (a) at the time integration of the finite element approximation of the k th Eq. (13), all order parameters η_l , ($l = 1, 2, \dots, k-1, k+1, \dots, n$) and stresses are known from the previous time step and fixed during the current time step; (b) at the time integration of the finite element approximation of the elasticity Eqs. (3), (12), (14), all order parameters are known from stage (a) and fixed during the current time step.

These assumptions correspond to an explicit time integration scheme and allow decoupling of the system Eqs. (3)–(14) at any small time step; i.e., any of the k th Eq. (13) and system (3), (12), (14) can be solved separately. For the solution to the k th Eq. (13) and system (3), (12), (14) at any time step, the finite element algorithms with implicit time-integration method for heat transfer problems and elasticity problems will be applied, respectively.

The finite element algorithm for the solution of Eqs. 3–14 at each time step is given in Box 2. The algorithm is implemented into the finite element program “FEAP” (Zienkiewicz and Taylor, 2000) for the 2-D and 3-D cases. The main advantages of the application

of the finite element method to the solution of the considered problem consist in the facts that the method is well developed for elasticity and heat transfer equations and that it can be easily applied to complicated geometry and boundary conditions.

Box 2. Finite element solution algorithm

Given: Initial values for stresses and order parameters at time t .

$$\{\sigma\}^t, \{\eta_k\}^t, \quad (k = 1, 2, \dots, n).$$

Find: Stresses and order parameters at time $t + \Delta t$.

$$\{\sigma\}^{t+\Delta t}, \{\eta_k\}^{t+\Delta t}, \quad (k = 1, 2, \dots, n).$$

1. Solve n “heat transfer” Eq. (13) separately in order to calculate the order parameters $\{\eta_k\}^{t+\Delta t}$ at time $t + \Delta t$.

$$[C] \left\{ \frac{d\eta_k}{dt} \right\} + [K_c] \{\eta_k\} = \{Q_k(\eta_1, \eta_2, \dots, \eta_n, \{\sigma\}^t)\}, \quad (k = 1, 2, \dots, n) \quad (20)$$

where $[C]$ is the “capacitance” matrix, $[K_c]$ is the “conductance” matrix, $\{Q_k\}$ is the load vector due to the source term.

2. Evaluate the transformation strain at $t + \Delta t$ (see Eq. (4))

$$\{\varepsilon_t\}^{t+\Delta t} = \{\varepsilon_t(\eta_1^{t+\Delta t}, \eta_2^{t+\Delta t}, \dots, \eta_n^{t+\Delta t})\}. \quad (21)$$

3. Solve the elastic problem Eqs. (3), (12), (14)

$$[M] \frac{d^2\{U\}}{dt^2} + [K]\{U\} = \{R(\eta_1^{t+\Delta t}, \eta_2^{t+\Delta t}, \dots, \eta_n^{t+\Delta t})\}, \quad (22)$$

where $[M]$ is the mass matrix, $[K]$ is the stiffness matrix, $\{U\}$ is the displacement vector, and $\{R\}$ is the load vector.

Update stresses at $t + \Delta t$

$$\{\sigma\}^{t+\Delta t} = [D]([B]\{U\}^{t+\Delta t} - \{\varepsilon_t\}^{t+\Delta t}) + \{\sigma^{in}\}, \quad (23)$$

where $[D]$ is the elastic modulus matrix, $[B]$ is the standard finite element B-matrix, σ^{in} are the initial stresses.

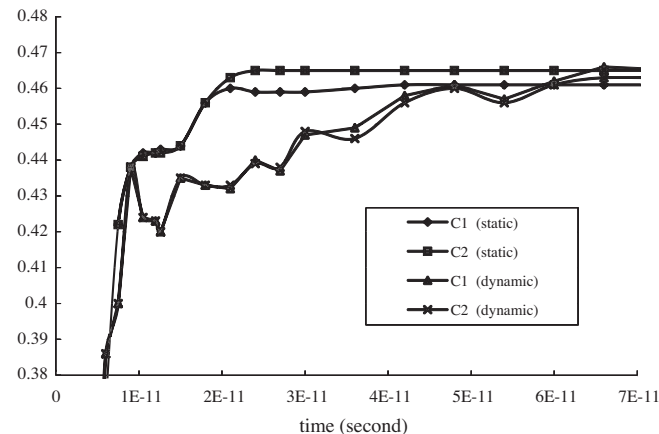


Fig. 9. Time dependence of the volume fraction of the martensitic phases, M_1 and M_2 , for the solution shown in Fig. 7 (dynamic) and Fig. 8 (static).

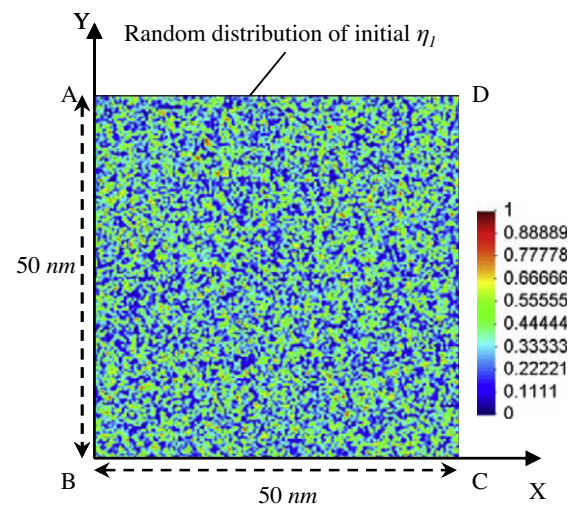


Fig. 10. A 2-D square specimen with the randomly distributed initial order parameters. Red represents martensitic variant 1 ($\eta_1 = 1$). Blue represents austenite or martensitic variant 2 ($\eta_1 = 0$). Other colors represent intermediate values between 0 and 1. (For interpretation of the references to colour in this figure legend, the reader is referred to the web version of this article.)

3.1. A test problem with a homogeneous solution

For the verification of the developed subroutine for the modeling of martensitic phase transformation, the following 2-D test problem at plane strain is considered for a homogeneous state. We assume zero inertial forces ($\rho \ddot{\mathbf{u}} = \mathbf{0}$) and homogeneous distribution of the order parameters, strains, and stresses over the two-dimensional plate shown in Fig. 1 for the solution of a phase transformation problem. Then, for the homogeneous static solution, Eqs. 3–14 can be simplified as follows. We assume that all order parameters except $\eta_1 = \eta$ are zero ($\eta_2 = \eta_3 = \dots = \eta_n = 0$) – i.e., one martensitic variant is considered. Then, Eq. (13) reduces to

$$\frac{\partial \eta}{\partial t} = -L \frac{\partial G(\eta, \sigma)}{\partial \eta}. \tag{24}$$

We select the following homogeneous initial conditions: $\eta^0 = 0.3$. The boundary conditions are given by Eq. (17) for the whole boundary; by Eq. (19) along the boundaries AB, BC, and CD (the fixed boundary); by Eq. (18) along the boundary AD (the free boundary); see Fig. 1. It is easy to show that at these boundary conditions, the following homogeneous stresses and strains can be found: $\varepsilon_{11} = 0$, $\sigma_{22} = 0$, $\sigma_{12} = 0$; also $\varepsilon_{33} = \sigma_{13} = \sigma_{23} = 0$ for the plane strain state. Then, using Hooke's law, two remaining stress components can be found from the following equations:

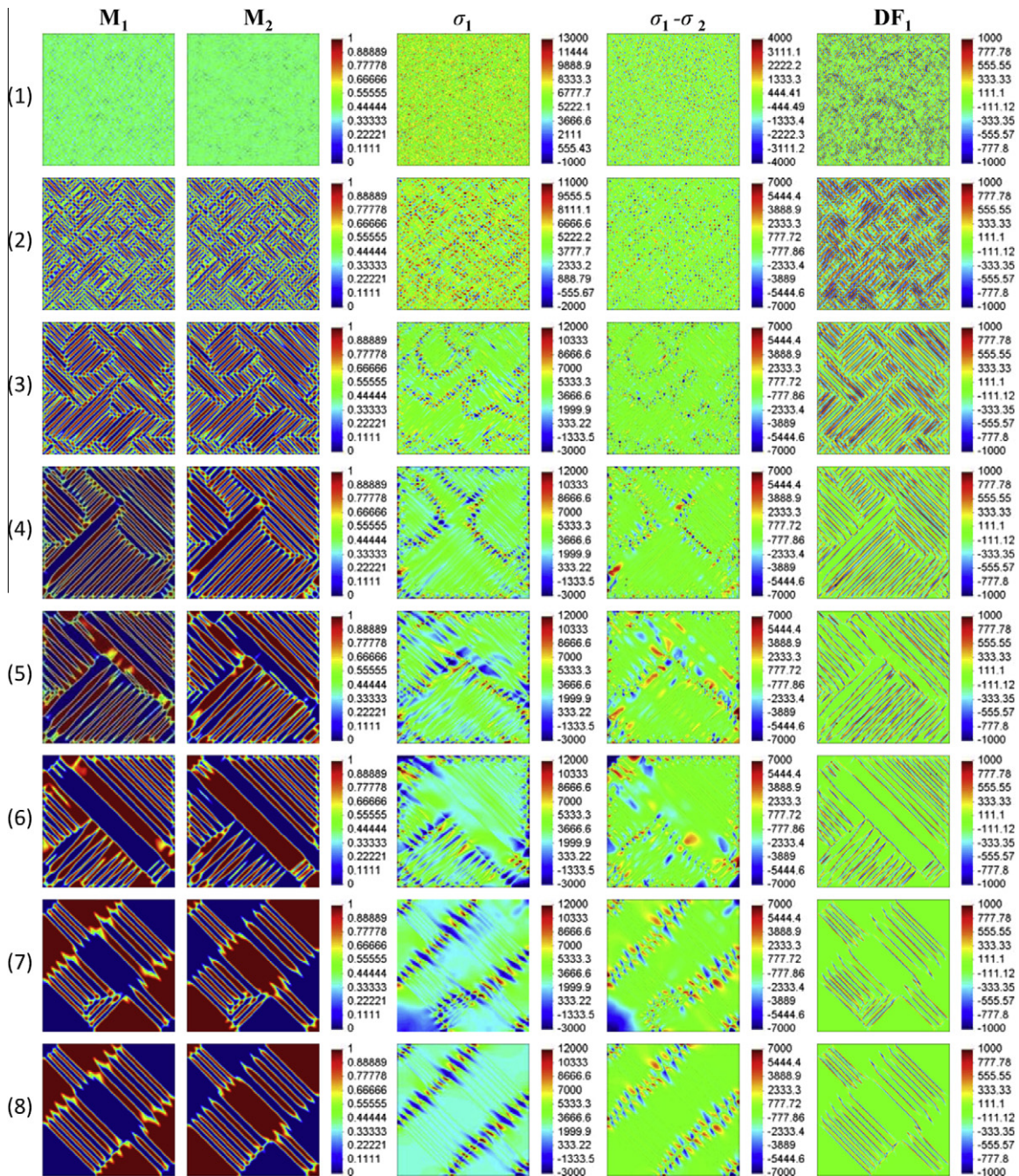


Fig. 11. Evolution of initially randomly distributed order parameters in a specimen for dynamic solution. Left two columns: η_1 and η_1 ; third and fourth columns: σ_1 and $\sigma_1 - \sigma_2$; right column: $\partial G / \partial \eta_1$, local driving force for evolution of η_1 . Rows (1)–(8) correspond to times 0.3 ps, 1.5 ps, 3.9 ps, 15 ps, 27 ps, 42 ps, 120 ps, and 420 ps, respectively.

$$\varepsilon_{11} = \frac{1}{E}(\sigma_{11} - \nu\sigma_{33}) + \varepsilon_{11}^t = 0, \quad \varepsilon_{33} = \frac{1}{E}(\sigma_{33} - \nu\sigma_{11}) = 0. \quad (25)$$

Therefore,

$$\sigma_{11} = -\frac{E\varepsilon_{11}^t}{1 - \nu^2}, \quad \sigma_{33} = -\frac{\nu E\varepsilon_{11}^t}{1 - \nu^2}, \quad (26)$$

where ε_{11}^t is a component of transformation strain (see Eq. (4)) that varies in time due to the time variation of the order parameter η . Thus, for the given homogeneous boundary and initial conditions, the solution of Eqs. (3)–(14) reduces to the solution of the evolution Eq. (24) with two non-zero stress components given by Eq. (26). The

integration of Eq. (24) yields the final homogeneous solution. The material parameters presented in Section 2 are used for the calculation of G and ε_{11}^t . For the simplification of the problem, only the first two non-zero components of the transformation strain in the first Eq. (16) are considered. The selected observation time $t = 4000$ ps is divided into 40,000 time steps with $\Delta t = 0.1$ ps.

We have solved this test problem at two different temperatures, 30 K and -100 K using the developed finite element code and the “Mathematica” code (WolframResearch, 2007). Because the solution is independent of the space coordinates, we use just one 2-D quadrilateral quadratic finite element. Fig. 2 shows that the finite element solution and the solution obtained by the “Mathematica”

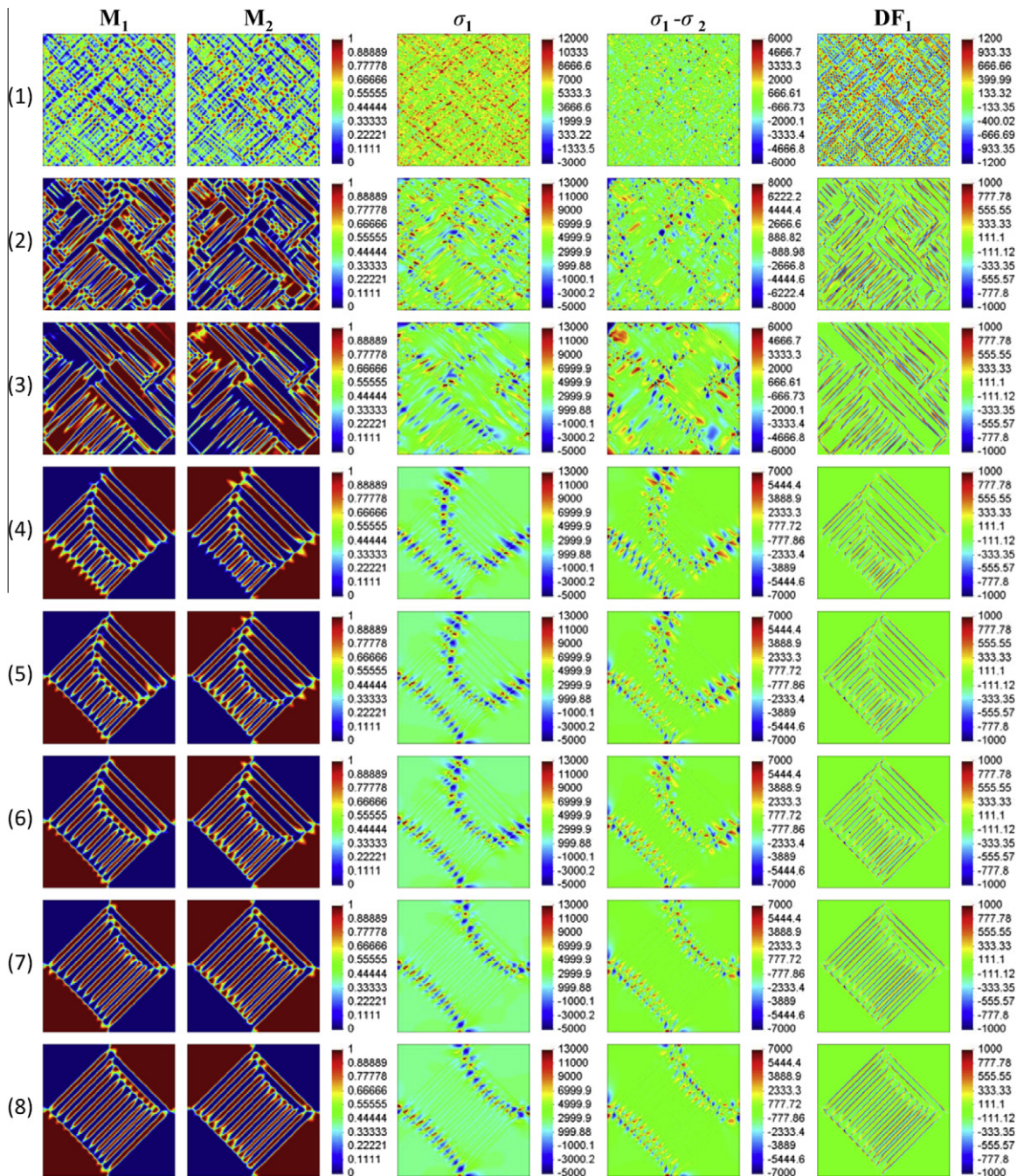


Fig. 12. Evolution of initially randomly distributed order parameters in a specimen for static solution. Left two columns: η_1 and η_2 ; third and fourth columns: σ_1 and $\sigma_1 - \sigma_2$; right column: $\partial G/\partial \eta_1$, local driving force for evolution of η_1 . Rows (1)–(8) correspond to times 0.3 ps, 1.5 ps, 3.9 ps, 15 ps, 27 ps, 42 ps, 120 ps, and 420 ps seconds, respectively.

code are practically the same for the two different temperatures. One of the temperatures was taken to be negative to demonstrate coincidence of solutions for a broad range of parameters; i.e., we showed that the solution of the same system of governing equations by two different approaches (by FEAP and by Mathematica) yields the same results for a broad range of parameters. These results were used for testing the developed code FEAP only. For the modeling of phase transitions in Section 4, the actual temperature is always positive.

It is necessary to mention that the code “FEAP” was also verified for the solution of non-homogeneous heat-transfer and elasticity problems. Therefore, we can expect that the code correctly solves Eqs. (3)–(14) for non-homogeneous solutions as well.

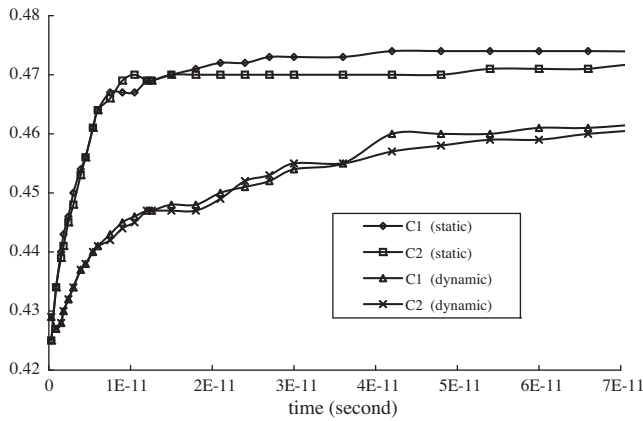


Fig. 13. Time dependence of volume fraction of the martensitic phases, M_1 and M_2 , for the solutions shown in Fig. 11 (dynamics) and Fig. 12 (quasi-static).

4. Numerical modeling

We will study the following model problems for the multi-variant martensitic phase transformation in a 2-D (plane strain) and 3-D specimens.

1. The 2-D modeling of the evolution of a thin, single-variant, martensitic nucleus, including the study of the effect of the variation of E and β on the evolution of the nucleus is considered in Section 4.1.
2. The 2-D modeling of multi-variant martensitic phase transformation in a single-crystal specimen including (a) the evolution of the initial martensitic embryo and (b) the evolution of the initial randomly distributed order parameters are considered in Section 4.2.

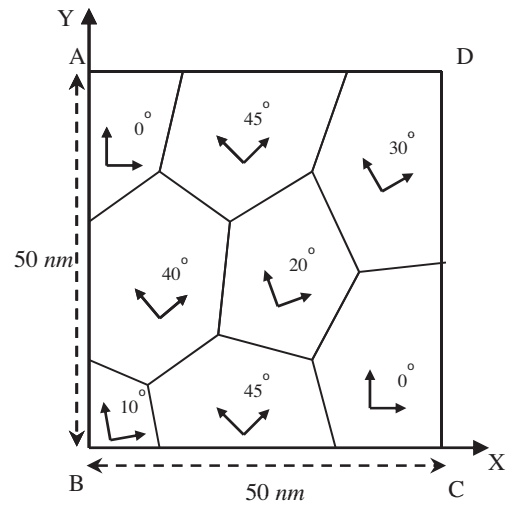


Fig. 15. 2-D polycrystalline specimen with 8 crystallites.

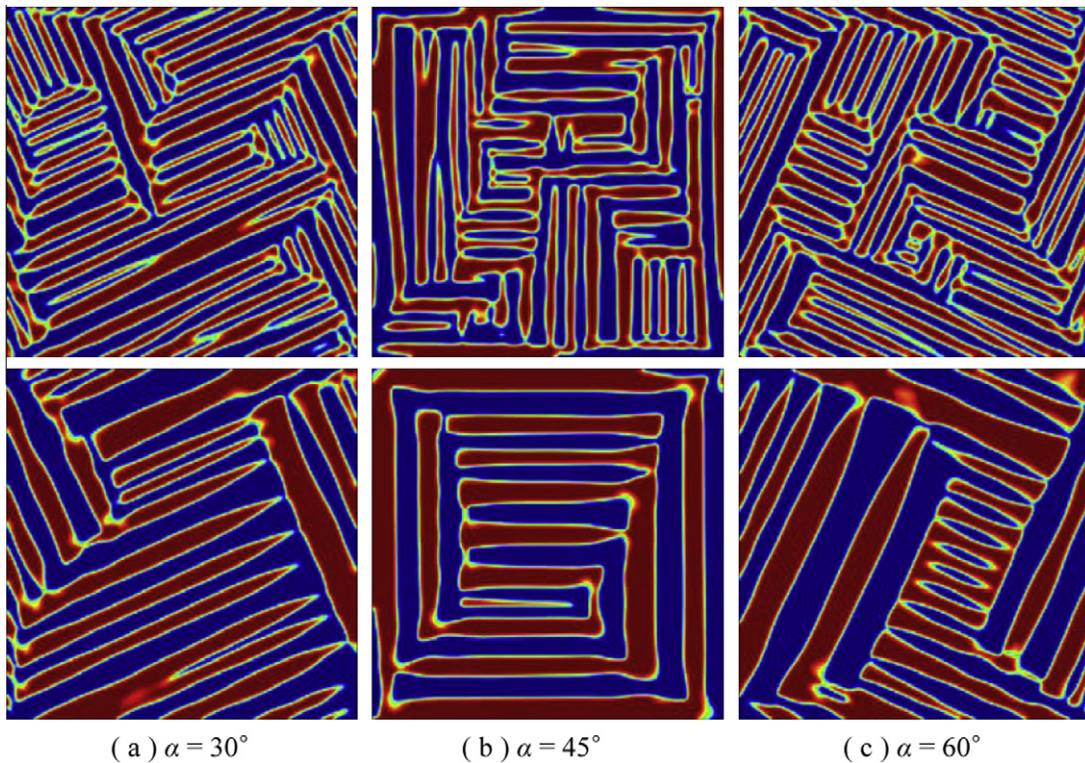


Fig. 14. The distribution of the order parameter η_1 in three specimens with different orientations of the crystal lattice at time 9.0 ps (top) and 75 ps (bottom). (a), (b), and (c) correspond to $\alpha = 30^\circ$, 45° , and 60° , respectively (dynamics).

3. Martensitic phase transformation in a 2-D polycrystalline specimen is considered in Section 4.3.
4. Martensitic phase transformation in a 3-D single crystal is considered in Section 4.4.
5. Martensitic phase transformation in 2-D single and polycrystalline specimens under impact loading is considered in Section 4.5.

4.1. Modeling of the evolution of a thin, single-variant martensitic nucleus

Let us consider the evolution of a thin, single-variant ($n = 1$ in Eq. (13)) martensitic nucleus in an austenitic 2-D plate shown in Fig. 3.

The dimensions of the plate are $50 \text{ nm} \times 50 \text{ nm}$. An initial thin, single-variant martensitic nucleus ($10.0 \text{ nm} \times 0.75 \text{ nm}$) is located at the center of the plate. The crystal lattice is rotated by 45° in the plane of the plate with respect to the Cartesian coordinate system shown in Fig. 3. Then the transformation strain in the Cartesian coordinate system is: $\varepsilon_{t1} = \{0.0685; 0.0685; -0.078; 0.1465; 0; 0\}$. We solve the problem for several different values of $E(193,800; 96,900; 38,760 \text{ MPa})$ and $\beta(2.33 \times 10^{-10}, 2.33 \times 10^{-11} \text{ N})$ for the analysis of their effect on the evolution of the nucleus. The dynamic and static formulations are considered.

The initial conditions for Eqs. (3)–(14) are as follows: (a) order parameter $\eta_1 = 0$ (which corresponds to austenite) for the whole specimen except the thin nucleus, where $\eta_1 = 1$ is given; (b) the

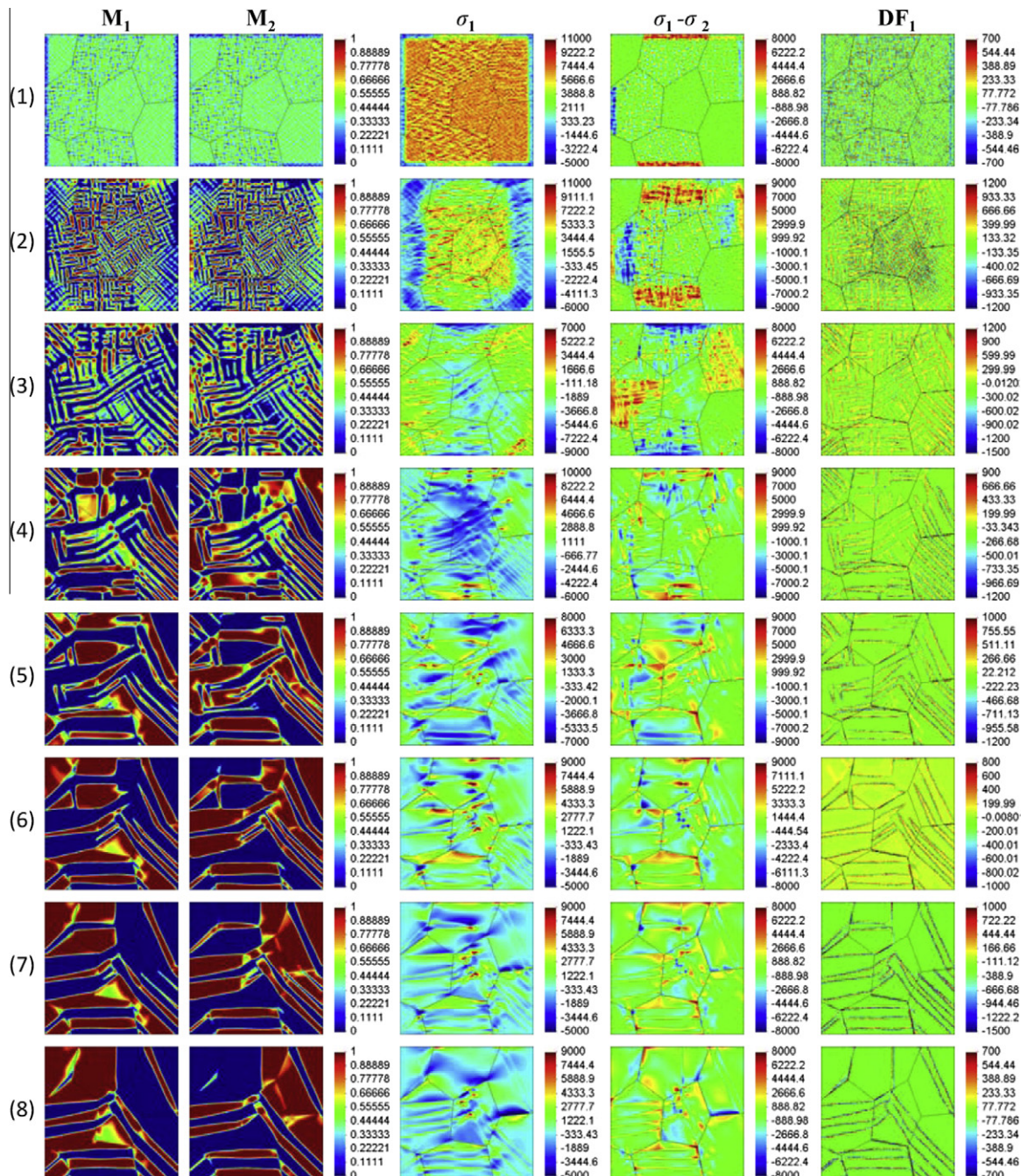


Fig. 16. Evolution of initially randomly distributed order parameters in a polycrystalline specimen for dynamic solution. Left two columns: η_1 and η_1 ; third and fourth columns: σ_1 and $\sigma_1 - \sigma_2$; right column: $\partial G / \partial \eta_1$. Rows (1)–(8) correspond to times 0.3 ps, 1.5 ps, 4.5 ps, 12 ps, 21 ps, 30 ps, 60 ps, and 420 ps, respectively.

initial displacement and velocity (prescribed for the dynamic case only) are zero for the whole specimen; (c) the initial homogeneous stresses ($\sigma_{11}^in = \sigma_{22}^in = 20 \text{ GPa}$) are applied to the whole specimen to promote phase transformation (see Eq. (23) in Box 2). The boundary conditions for the entire boundary are presented by Eqs. (17) and (18) (the free boundary). The homogeneous constant temperature $\theta = 288 \text{ K}$ is assumed. A structured finite element mesh consisting of 22,500 (150×150) quadratic, eight-node, rectangular finite elements and 68,101 nodes is used for calculation. The observation time $\tilde{t} = 21 \text{ ps}$ is subdivided into 700 time steps with the time increment $\Delta t = 0.03 \text{ ps}$.

The comparison of the numerical solutions for static and dynamic formulations for NiAl is shown in Fig. 4. The effect of E and β on the evolution of the nucleus is shown in Fig. 5. It is visible from Figs. 4 and 5 that the thin nucleus rotates through a constant angle of about 15° during the initial stage of evolution. For comparison, the invariant plane (i.e., the plane that is not deformed for the given transformation strain tensor) is inclined under 15.13° , which is quite close. Thus, rotation of interface is caused by reduction of the energy of internal stresses due to transformation strain. Note that the explicit expression for the driving force for interface rotation is derived in Levitas and Ozsoy (2009a,b). Stresses are concentrated at the sharp ends of the nucleus, causing some incomplete transformation to reduce elastic energy.

The growth rate for the static case is faster than that for the dynamic case both in lengthening and widening directions (Fig. 4). This is a consequence of material inertia during growing transformation strain at each transforming point. After the nucleus reached lateral sides of a sample, the static solution exhibits straight interfaces, while for the dynamic case transformation propagates faster near free surface because of smaller inertia.

The evolution of the single-variant martensitic nucleus for different values of E and β is shown in Fig. 5. Comparing the first two columns with the same E , we can evaluate the effect of β . For plane interface, interface width δ and velocity v are proportional to $\sqrt{\beta}$ (Levitas et al., 2010). For $\beta = 2.33 \times 10^{-10} \text{ N}$, interface

width is larger than initial width of the nucleus. That is why the nucleus first evolves to the closest energy-minimizing configuration, namely reducing the value of η , increasing the width, and optimizing the orientation. After this, the opposite process occurs – i.e., η increases and reaches 1 in the nucleus, but the width is reduced. Finally, when free surface is reached, widening starts. The fact that nucleus evolution is more pronounced for smaller β does not contradict the relationship $v \sim \sqrt{\beta}$ because the stage of stationary interface propagation was not reached for larger β . Surface energy of the nucleus is also $\sim \sqrt{\beta}$, thus larger β suppresses the nucleation stage, and that is what is observed in Fig. 5.

Comparing the second, third, and fourth columns for the same β and different Young moduli E , we can evaluate the effect of E . Reduction in E reduces the contribution of the elastic energy in comparison with the surface energy and causes faster thickening but slower growth in a longitudinal direction. The nucleus possesses parallelogram shape (rather than ellipsoidal shape assumed in simplified analytical approaches based on Eshelby solution) with all sides close to invariant planes. After reaching free surface, for large E , the nucleus advances more along the free surface, while for smaller E it has a slightly curved interface, with thickening from the center to the free surfaces.

4.2. Modeling of multi-variant martensitic phase transformation in a 2-D single-crystalline specimen

4.2.1. Evolution of the initial martensitic embryo

Let us consider the evolution of the initial square martensitic embryo ($2.5 \text{ nm} \times 2.5 \text{ nm}$) in a 2-D square specimen of $50 \text{ nm} \times 50 \text{ nm}$ shown in Fig. 6. Two martensitic variants will be considered ($n = 2$ in Eq. (13)).

The initial conditions are: (a) zero order parameters, $\eta_1 = \eta_2 = 0$ (which correspond to austenite), for the whole specimen except the initial multi-variant martensitic embryo, where the order parameters $\eta_1 = \eta_2 = 0.5$ are given; (b) zero initial displacements and velocities (which have to be prescribed for the dynamic case only) for the whole specimen; (c) the initial homogeneous stresses ($\sigma_{11}^in = \sigma_{22}^in = 20 \text{ GPa}$) are applied to the whole specimen to promote phase transformation (see Eq. (23) in Box 2). The boundary conditions are given by Eqs. (17) and (19) (the fixed boundary without friction). The homogeneous constant temperature $\theta = 288 \text{ K}$ is assumed, and the observation time $\tilde{t} = 420 \text{ ps}$ is subdivided into 14,000 time steps with a time increment $\Delta t = 0.03 \text{ ps}$. A structured finite element mesh with 22,500 (150×150) quadratic eight-node rectangular finite elements and 68,101 nodes is used in the calculations.

The evolution of the martensitic embryo (η_1 and η_2), the stresses σ_1 and $\sigma_1 - \sigma_2$, and the local driving force $\partial G / \partial \eta_1$ for evolution of η_1 are shown in Fig. 7 for the dynamic formulation and in Fig. 8 for the static formulation at times 0.3 ps, 1.5 ps, 6.0 ps, 15 ps, 27 ps, 42 ps, 60 ps, and 420 ps, respectively. Below, these times will be called stages (1)–(8). Let us analyze the evolution of the embryo. Initially, square martensitic embryo grows faster in the vertical direction for \mathbf{M}_1 and in the horizontal direction for \mathbf{M}_2 ; see stages (1) and (2). Then the martensitic embryo splits into two variants and forms a finely twinned martensitic structure. The directions of martensitic strips are under 45° to coordinate axes, which coincides with those determined from crystallography theory (Bhattacharya, 2003). Different twinned martensite structures are in contact along symmetry axes of a sample. Further growth occurs by propagation of four austenite-twinned martensite interfaces until the entire sample transforms into twinned martensite microstructure, stage (4) for both cases. During stages (1)–(4), there are no essential differences between the dynamic and static cases, although for the static formulation, the growth rate is a little bit faster than for the dynamic one.

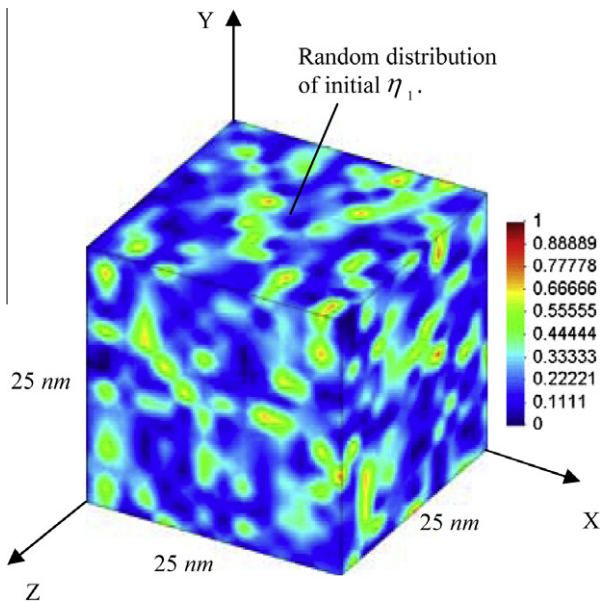


Fig. 17. A 3-D cubic specimen with the random distribution of initial order parameter η_1 . Red represents martensitic variant 1 ($\eta_1 = 1$). Blue ($\eta_1 = 0$) represents austenite or other martensitic variants or the mixture of austenite and other martensitic variants. Other colors represent intermediate values between 0 and 1 and correspond to the mixture of austenite and martensite. (For interpretation of the references to colour in this figure legend, the reader is referred to the web version of this article.)

Then coalescence (coarsening) of martensitic plates occurs, which reaches the stationary state for the static case in stage (5) after $t \approx 21$ ps. Stationary microstructure exhibits quite large triangles and rectangles, along with thin plates. For dynamic loading, in stages (5)–(8) the microstructure gradually changes and reaches the stationary state at $t \approx 80$ ps. The final microstructures for the dynamic and static cases have similar shapes (four triangle regions at the corners of the specimen and four similar regions near the central region of sides of the square), but they are not the same. The martensitic strips in the clusters of the twin structure are thicker for the dynamic case than for the static case. We

define the volume fraction of each martensitic variant by the equation

$$c_i = \frac{\text{Number of nodes at which } \eta_i = 1}{\text{Total number of nodes}} \quad (27)$$

This equation provides good approximations of volume fractions when a fine uniform mesh is used for the finite element solution. Note that the difference $1 - c_1 - c_2$ represents a concentration of austenite and the interface regions, and, after austenite has disappeared, just the concentration of interface regions. The evolution of the volume fraction of the martensitic phases, M_1 and M_2 , for

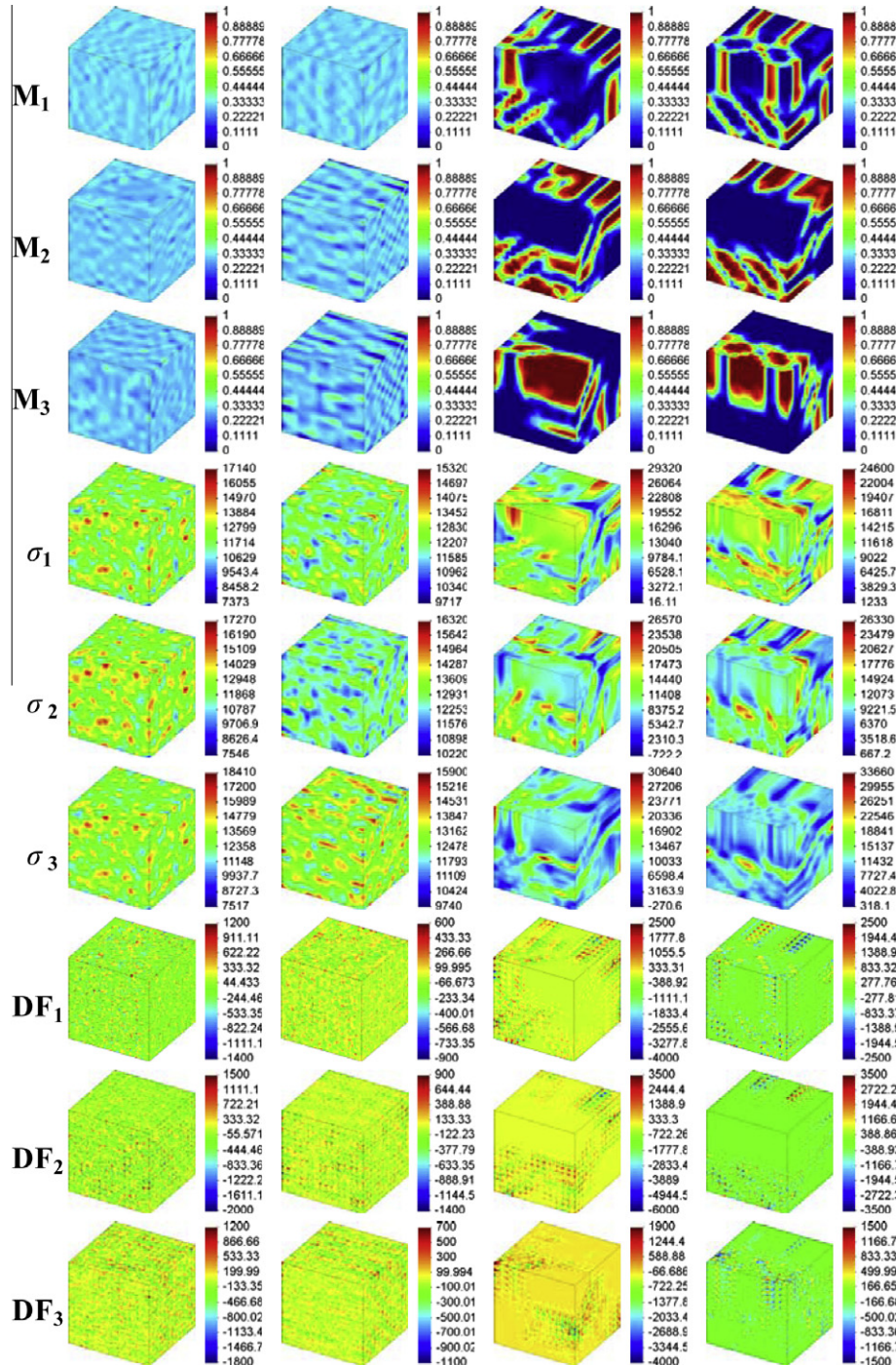


Fig. 18. Evolution of microstructure in the 3-D specimen for dynamic solution. First three rows: η_1 , η_2 , and η_3 ; fourth to sixth rows: σ_1 , σ_2 , and σ_3 ; seventh to ninth rows: $\partial G/\partial \eta_1$, $\partial G/\partial \eta_2$, and $\partial G/\partial \eta_3$, the local driving forces for evolution η_1 , η_2 , and η_3 . Columns 1–4 correspond to times 0.3 ps, 1.5 ps, 48 ps, and 420 ps, respectively.

the dynamic and static cases is shown in Fig. 9. A very sharp increase of concentration of both martensitic phases until time $t \approx 10$ ps is observed, since a martensitic embryo grows and the specimen is filled with martensitic strips. There are no significant differences between the dynamic and static cases and between martensitic variants during this period. However, after that, the curves split. For static formulations, volume fraction grows faster and more smoothly, and the concentration of M_1 becomes visibly higher than for M_2 ; sharp growth at $15 \text{ ps} \leq t \leq 23 \text{ ps}$ corresponds to a sudden change of microstructure (see stages (4) and (5) in Fig. 8). For dynamic formulation, there are several drops in concen-

tration of martensitic variants (i.e., reverse transformation occurs), the growth in general is slower than that for static formulation, and the difference between variants is negligible.

4.2.2. Evolution of the randomly distributed initial order parameters

We consider the evolution of the randomly distributed initial order parameters in the 2-D specimen. The random numbers between zero and unity are assigned to the nodal values of the initial order parameters ($0 < \eta_1, \eta_2 < 1$) in each node of the finite element mesh using the built-in FORTRAN function “RANDOM” (see Fig. 10). The other initial and boundary conditions for Eqs. 3–14

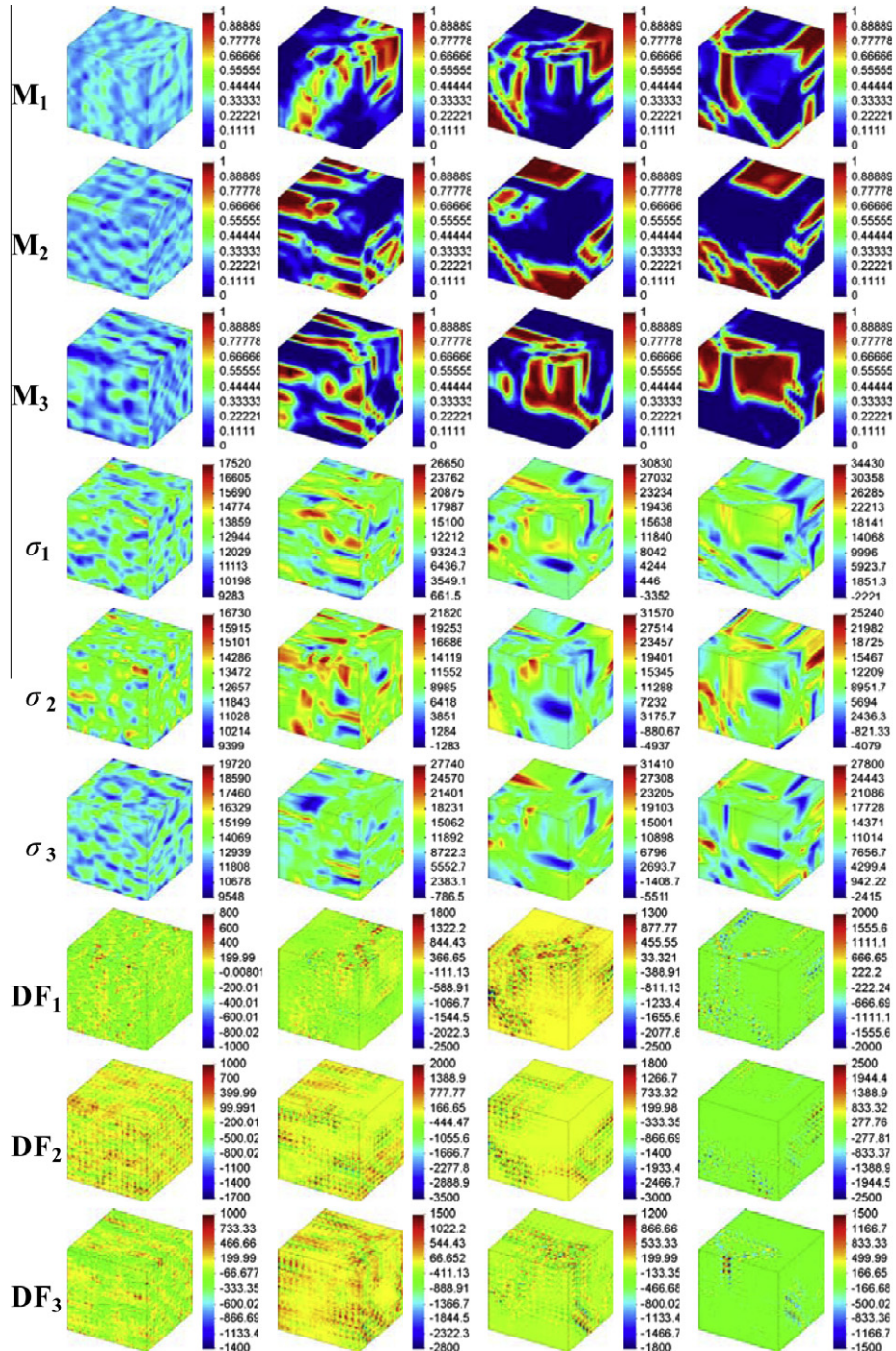


Fig. 19. Evolution of microstructure in the 3-D specimen for the static solution. First three rows: η_1 , η_2 , and η_3 ; fourth to sixth rows: σ_1 , σ_2 , and σ_3 ; seventh to ninth rows: $\partial G/\partial \eta_1$, $\partial G/\partial \eta_2$, and $\partial G/\partial \eta_3$, the local driving forces for evolution η_1 , η_2 , and η_3 . Columns 1–4 correspond to times 0.3 ps, 1.5 ps, 48 ps, and 420 ps, respectively.

for this problem are the same as those for the previous problem in Section 4.2.1.

The evolution of the microstructure for the dynamic and static formulations is shown in Figs. 11 and 12. The evolution for the static case is much faster than that for the dynamic case; e.g., see M_1 and M_2 at stage (1) for the dynamic case in Fig. 11 and for the static case in Fig. 12. At stage (1), the randomly distributed initial order parameters form several martensitic plates for the static formulation, while there are only intermediate values of the order parameters ($\eta_1 \approx \eta_2 \approx 0.5$) in the whole specimen in the dynamic case. Also, in the static case, the microstructure converges faster to the final stationary microstructure (at time $t \approx 125$ ps) than that in the dynamic case (at time $t \approx 170$ ps). Next, for the dynamic and static cases, the corresponding microstructures have different evo-

lution histories. For the static case, the microstructure changes significantly at $t \approx 6.0$ ps (see stages (3) and (4) in Fig. 12) and the microstructure at stage (4) is very similar to the final stationary microstructure. The final microstructures for the dynamic and static case are totally different as well (see stage (8) in Figs. 11 and 12). The evolution of the volume fraction of martensitic variants in Fig. 13 also shows much faster progress for static formulation.

4.3. Martensitic phase transformation in a 2-D polycrystalline specimen

In the 2-D case, the orientation of each grain is described by the angle α between the local Cartesian system related to the grain and the Cartesian system related to the specimen. The transformation strains for each grain given in the local Cartesian system (related to the grain) is recalculated in the global Cartesian system used in calculations as follows:

$$[\epsilon_{ti}^{gf}] = [\alpha]^t [\epsilon_{ti}] [\alpha]. \tag{28}$$

Here, $[\alpha]$ is the rotation matrix corresponding to the rotation through angle α about the z-axis; $[\epsilon_{ti}]$ for the 2-D case with two martensitic variants ($i = 1, 2$) are given by the first two Eq. (16) with the first four strain components. In order to study the effect of the crystal lattice orientation with respect to the geometry of the specimen on phase transformation, we first consider the evolution of the initial martensitic embryo for three single-crystal specimens of size $50 \text{ nm} \times 50 \text{ nm}$ (similar to the problems in Section 4.2) with different orientations of the crystal lattice characterized by different angles $\alpha = 30^\circ, 45^\circ,$ and 60° . We use the same material properties and the same initial and boundary conditions as those in Section 4.2. The microstructures in the three specimens are shown in Fig. 14 at times $t = 9.0$ ps and $t = 75$ ps. As can be seen, the microstructures of three different specimens consist of a number of parallel and perpendicular martensitic plates. The orientations of the martensitic plates are different due to the different orientations of crystal lattice. However, in all cases plates are under 45° to the cubic axis, which is in good agreement with the crystallography theory (Bhattacharya, 2003).

Next, let us consider martensitic phase transformation in the 2-D polycrystalline specimen shown in Fig. 15. The $50 \text{ nm} \times 50 \text{ nm}$ square polycrystalline specimen is assumed to have eight grains. Different orientations for the grains are represented by

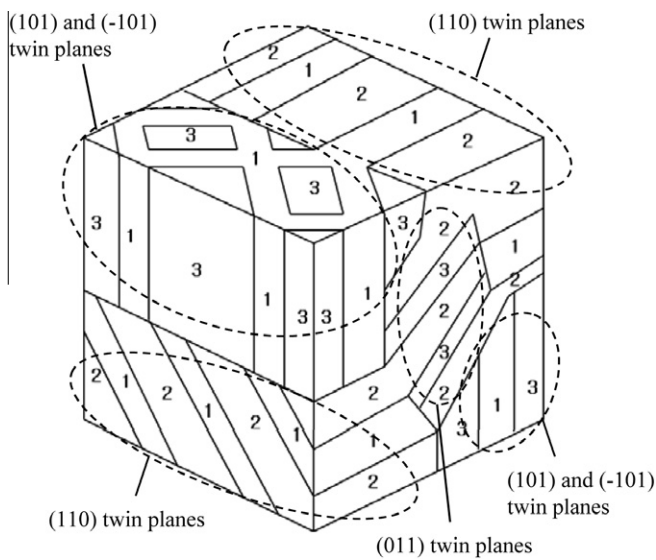


Fig. 20. Schematic diagram of martensitic microstructure for the dynamic formulation at the final time instant, which contains all three martensitic variants. The sample is divided into several regions consisting of two martensitic variants in twin relations. Designated planes between the twin-related variants coincide with those determined from the crystallographic theory (Idesman et al., 2008).

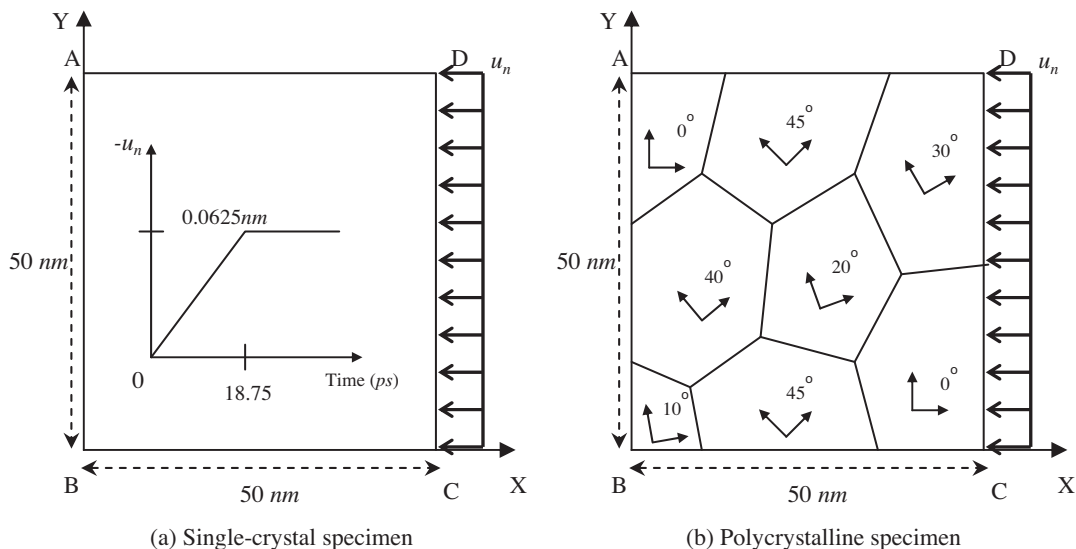


Fig. 21. Single- and polycrystal specimens under impact loading along boundary CD.

assigning the different values of the angle α ; see Fig. 15. The corresponding transformation strains for each grain are calculated according to Eq. (28). The boundary conditions, the initial conditions, and the material parameters are the same as those for the previous problems in Section 4.2.2. The dynamic formulation is considered only, and an unstructured finite element mesh with 40,374 quadratic six-node triangular finite elements and 81,283 nodes is used in the calculations. Comparing the results for different mesh types and the number of degrees of freedom (see Figs. 16 and 11), we found that the thickness of the interfaces is practically the same when it contains 3–4 finite elements – i.e., solutions are mesh-independent.

Let us analyze the results of calculations shown in Fig. 16. First, at stages (1) and (2), randomly distributed initial order parameters form a complicated tweed structure, which is not transformed to complete martensite yet ($0 < \eta_i < 1$). The directions of the tweeds in each grain are different from each other because each grain has a different crystal lattice orientation. As transformation continues (see stages (2)–(5)), several thin martensitic plates are merged or have disappeared, and the polycrystalline specimen entirely changes to the complete martensitic variants except some small regions, where the evolution still progresses. During stages (6)–(8), coalescence is almost completed, and there are only small, local variations of order parameters. Throughout the transformation process, the directions of the plates

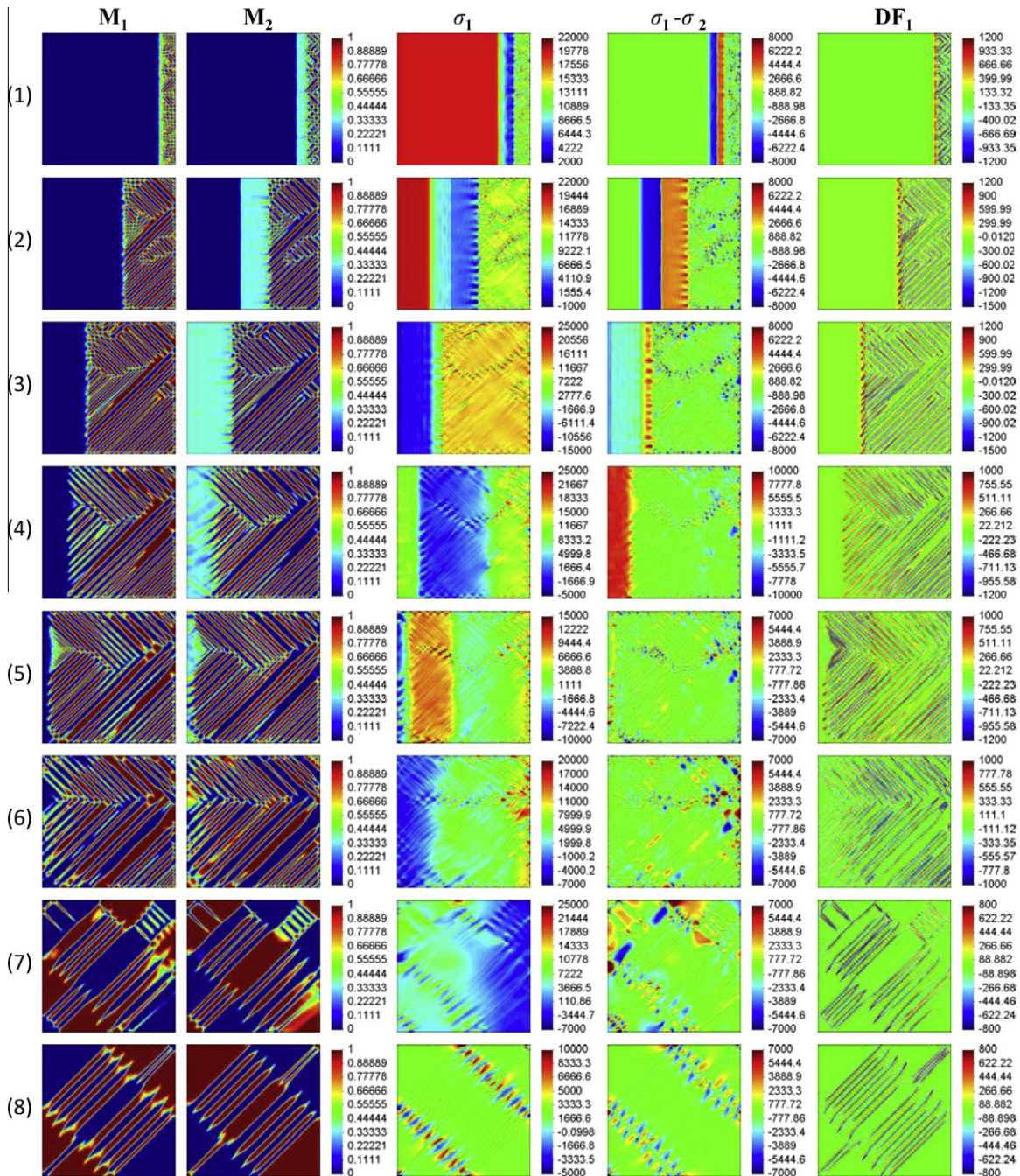


Fig. 22. Evolution of microstructure in a single-crystal specimen under impact loading at the right side of the boundary. Left two columns: η_1 and η_2 ; third and fourth columns: σ_1 and $\sigma_1 - \sigma_2$; right column: $\partial G/\partial \eta_1$, local driving force for evolution of η_1 . Rows (1)–(8) correspond to times 1.8 ps, 5.4 ps, 9 ps, 12.6 ps, 15 ps, 24 ps, 60 ps, and 420 ps, respectively.

in each grain are consistent with crystallographic theory and do not change. Some of the martensitic plates, which pass across the grain boundary, are bent at the boundary according to change in the orientation of the crystal lattice, and some other martensitic plates do not penetrate the neighboring grains.

4.4. Martensitic phase transformation in a 3-D single-crystalline specimen

The cubic to tetragonal martensitic transformation in a 3-D specimen will be considered in this section. Fig. 17 shows a 3-D cubic specimen with dimensions 25 nm × 25 nm × 25 nm that may consist of austenite and three martensitic variants ($n = 3$). The ini-

tial conditions are as follows: (a) the random distribution of the initial order parameters $\eta_1, \eta_2,$ and η_3 with values between 0 and 1 was prescribed (similar to that in Section 4.2.2); (b) initial displacements and velocities (which have to be prescribed for the dynamic case only) are zero for the whole specimen; (c) homogeneous initial stresses ($\sigma_{11}^i = \sigma_{22}^i = \sigma_{33}^i = 20$ GPa and $\sigma_{12}^i = \sigma_{13}^i = \sigma_{23}^i = 0$) are applied to the whole specimen for the promotion of transition. The boundary conditions are described by Eqs. (17) and (19) (the fixed boundary without friction). We also assume the homogeneous temperature $\theta = 288$ K, which does not change during phase transformation. The observation time $\tilde{t} = 420$ ps, during which the microstructure reaches the stationary state, is subdivided into 14,000 time steps with the time increment $\Delta t = 0.03$ ps. A structured finite element mesh with 2028 quadratic

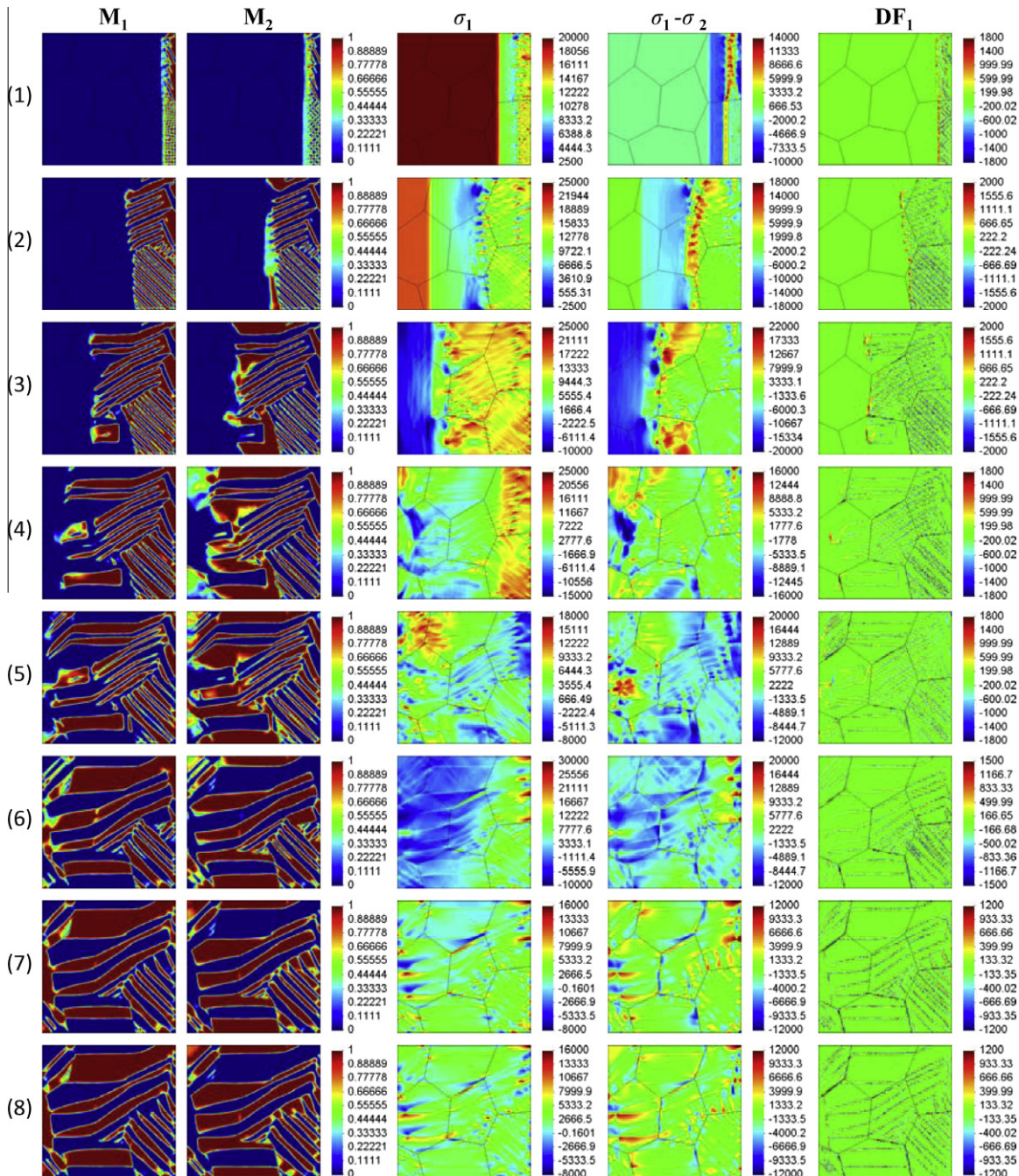


Fig. 23. Evolution of microstructure in a polycrystalline specimen under impact loading at the right side of boundary. Left two columns: η_1 and η_2 ; third and fourth columns: σ_1 and $\sigma_1 - \sigma_2$; right column: $\partial G / \partial \eta_1$. Rows (1)–(8) correspond to times 1.8 ps, 5.4 ps, 9 ps, 12.6 ps, 15 ps, 24 ps, 60 ps, and 420 ps, respectively.

27-node brick finite elements and 18,225 nodes is used in the calculations.

The results of the evolution of microstructure for the static and dynamic formulations are shown in Figs. 18 and 19. Similar to the 2-D problem in Section 4.2.2, the rate of a microstructure transformation from austenite to martensite is much faster for the static formulation than for the dynamic formulation; see the order parameters in the second columns in Figs. 18 and 19. For the static formulation, the randomly distributed initial order parameters form microstructure with several martensitic plates at time $t = 1.5$ ps. However, at the same time in the dynamic formulation, only intermediate values between 0 and 1 of the order parameters occur in the whole specimen. For the static and dynamic formulations, the corresponding microstructures have different evolution histories, and the stationary microstructures at the considered observation times are totally different; see the order parameters in the fourth columns in Figs. 18 and 19.

Fig. 20 shows the schematic diagram of the stationary martensitic microstructure for the dynamic case at the final time (all three martensitic variants are shown in one figure). The sample is divided into several regions consisting of two martensitic variants, which are in twin relations. Planes between twin-related variants are designated in Fig. 20 and coincide with those determined from the crystallographic theory; see Bhattacharya (2003).

4.5. Martensitic phase transformation in 2-D single- and polycrystal specimens under impact loading

Single- and polycrystal specimens under impact loading at the boundary CD shown in Fig. 21 are considered. The initial conditions are: (a) zero order parameters $\eta_1 = \eta_2 = 0$ (which correspond to austenite) in the whole specimen except the nodal values at the boundary CD, where random non-zero values ($0 < \eta_1, \eta_2 < 0.3$) are given; (b) zero initial displacements and velocities for the whole specimen; the initial homogeneous stresses ($\sigma_{11}^i = \sigma_{22}^i = 20$ GPa). The boundary conditions are given as follows: (a) by Eq. (17) along the entire boundary of the specimen; (b) by Eq. (19) at the boundaries AB, BC, and AD (the fixed boundary without friction); impact loading $u_n = -1/300t$ for $0 \leq t \leq 18.75$ ps and $u_n = -0.0625$ nm for $t > 18.75$ ps (see Fig. 21(a)) and $\tau_n = 0$ at the boundary CD.

Figs. 22 and 23 show the results for single- and poly-crystal specimens. For the single-crystal specimen (Fig. 22), the stresses due to impact loading and nucleation sites at the boundary lead to the phase transformation. The wave front of propagating elastic wave follows by the region in which $\eta_2 \simeq 0.33$ and $\eta_1 = 0$, then by region with $\eta_2 \simeq 0.33$, but \mathbf{M}_1 is completely or almost completely formed, and finally by region of twinned martensite. Reflected wave does not produce significant changes, and coalescence and increase in size of typical martensitic units takes place, similar to the results for the problem in Fig. 11.

For a polycrystalline specimen under impact loading (Fig. 23), phase transformation starts from the right part of the specimen as well. The elastic wave propagates with the same rate because elastic anisotropy is neglected. Phase transformation front propagates with rates close to that in the single crystal, but its structure is different. Thus, the region with the constant but incomplete $\eta_2 \simeq 0.33$ is very small and then disappears. Both variants propagate approximately with the same rate as a combined twinned martensite structure. Orientation of each martensite-martensite interface is close to 45° with respect to the local cubic axes. Also, coalescence of the nearest martensitic units of the same variant with disappearance of an alternative martensitic variant leads to the reduction in number of martensitic plates.

5. Concluding remarks

In the paper, an advanced finite element approach for the phase-field modeling of the dynamics of multivariant martensitic phase transformation at the nanoscale is developed. Since characteristic time of occurring of phase transformation in the material point is of the order of magnitude of 1 ps and transformation strain is of the order of magnitude of 0.1, it is not surprising that material inertia makes a significant contribution even when there is no dynamic mechanical loading. Thus, for the traditional problems on relaxation of initial embryo or stochastic perturbations to the stationary microstructure without any external nonstationary loading, for both 2-D and 3-D formulations, the dynamic solution relaxes more slowly to the stationary state than does the static one, and it also exhibits in some cases dynamic rearrangements of the microstructure with oscillating concentrations of martensitic variants – i.e., with some reverse transformation stages. For growth and reorientation of a single single-variant martensitic nucleus, the effect of dynamics, elastic properties, and gradient (i.e., interface) energy was studied at different growth stages. The effects of single-crystal lattice orientation and polycrystalline structure is elucidated as well. For dynamic loading of single- and polycrystalline samples, nontrivial transformation fronts are found. Despite the completely different constitutive models, some of our microstructures qualitatively resemble those in Lookman et al. (2003a,b).

In the future work, the current model will be further advanced by taking into account interface tension and controllable martensite-martensite energy (Levitas and Javanbakht, 2010), athermal threshold (Levitas and Lee, 2007; Levitas et al., 2010), large-strain formulation (Levitas et al., 2009), and temperature variation.

Acknowledgments

AVI and JYC's research has been supported in part by the Texas Tech University. AVI also acknowledges support of Air Force Office of Scientific Research. JYC and TP acknowledge support of the Hanyang University, Seoul, Korea, under the World Class University project funded by the National Research Foundation of Korea. VIL acknowledges support of National Science Foundation, Army Research Office, and Defence Threat Reduction Agency.

References

- Ahluwalia, R., Lookman, T., Saxena, A., Bishop, A., 2003. Elastic deformation of polycrystals. *Phys. Rev. Lett.* 91 (055501), 1–4.
- Artemev, A., Wang, Y., Khachatryan, A., 2000. Three-dimensional phase field model and simulation of martensitic transformation in multilayer systems under applied stresses. *Acta Mater.* 48 (10), 2503–2518.
- Artemev, A., Jin, Y., Khachatryan, A., 2001. Three-dimensional phase field model of proper martensitic transformation. *Acta Mater.* 49 (7), 1165–1177.
- Bhattacharya, K., 2003. *Microstructure of Martensite: Why It Forms and How It Gives Rise to the Shape-Memory Effect*. Oxford University Press, New York.
- Curnoe, S., Jacobs, A., 2001a. Statics and dynamics of domain patterns in hexagonal-orthorhombic ferroelastics. *Phys. Rev. B* 63 (094110).
- Curnoe, S., Jacobs, A., 2001b. Time evolution of tetragonal-orthorhombic ferroelastics. *Phys. Rev. B* 64 (064101).
- Ichitsubo, T., Tanaka, K., Koiwa, M., Yamazaki, Y., 2000. Kinetics of cubic to tetragonal transformation under external loadings. *Phys. Rev. B* 62 (9), 5435–5441.
- Idesman, A., Levitas, V., Preston, D., Cho, J.-Y., 2005. Finite element simulations of martensitic phase transitions and microstructure based on strain softening model. *J. Mech. Phys. Solids* 53 (3), 495–523.
- Idesman, A.V., Cho, J.-Y., Levitas, V.I., 2008. Finite element modeling of dynamics of martensitic phase transitions. *Appl. Phys. Lett.* 93, 043102.
- Jacobs, A., 2000. Landau theory of structures in tetragonal-orthorhombic ferroelastics. *Phys. Rev. B* 61, 6587–6595.
- Jacobs, A., Curnoe, S., Desai, R., 2003. Simulations of cubic-tetragonal ferroelastics. *Phys. Rev. B* 68, 224104.
- Levitas, V., Javanbakht, M., 2010. Surface tension and energy in multivariant martensitic transformations: Phase-field theory, simulations, and model of coherent interface. *Phys. Rev. Lett.* 105, 165701.

- Levitas, V., Javanbakht, M., 2011a. Phase-field approach to martensitic phase transformations: Effect of martensite-martensite interface energy. *Int. J. Mater. Res.* 102 (6), 652–665.
- Levitas, V., Javanbakht, M., 2011b. Surface-induced phase transformations: Multiple scale and mechanics effects and morphological transitions. *Phys. Rev. Lett.* 107, 175701.
- Levitas, V., Lee, D.-W., 2007. Athermal resistance to an interface motion in phase field theory of microstructure evolution. *Phys. Rev. Lett.* 99, 245701.
- Levitas, V., Ozsoy, I.B., 2009a. Micromechanical modeling of stress-induced phase transformations. Part 1. Thermodynamics and kinetics of coupled interface propagation and reorientation. *Int. J. Plast.* 25 (2), 239–280.
- Levitas, V., Ozsoy, I.B., 2009b. Micromechanical modeling of stress-induced phase transformations. Part 2. Computational algorithms and examples. *Int. J. Plast.* 25 (3), 546–583.
- Levitas, V., Preston, D., 2002a. Three-dimensional Landau theory for multivariant stress-induced martensitic phase transformations. part i. austenite \leftrightarrow martensite. *Phys. Rev. B* 66 (1–9), 134206.
- Levitas, V., Preston, D., 2002b. Three-dimensional Landau theory for multivariant stress-induced martensitic phase transformations. Part ii. Multivariant phase transformations and stress space analysis. *Phys. Rev. B* 66 (1–15), 134207.
- Levitas, V., Samani, K., 2011a. Coherent solid-liquid interface with stress relaxation in a phase-field approach to the melting/freezing transition. *Phys. Rev. B, Rapid Commun.* 84 (14), 140103(R).
- Levitas, V., Samani, K., 2011b. Size and mechanics effects in surface-induced melting of nanoparticles. *Nature Commun.* 2 (284).
- Levitas, V., Preston, D., Lee, D.-W., 2003. Three-dimensional Landau theory for multivariant stress-induced martensitic phase transformations. part iii. alternative potentials, critical nuclei, kink solutions, and dislocation theory. *Phys. Rev. B* 68, 134201.
- Levitas, V., Idesman, A., Preston, D., 2004. Microscale simulation of evolution of martensitic microstructure. *Phys. Rev. Lett.* 93, 105701.
- Levitas, V., Lee, D.-W., Preston, D., 2006. Phase field theory of surface- and size-induced microstructures. *Europhys. Lett.* 76, 81–87.
- Levitas, V., Levin, V., Zingerman, K., Freiman, E., 2009. Displacive phase transitions at large strains: Phase-field theory and simulations. *Phys. Rev. Lett.* 103, 025702.
- Levitas, V., Lee, D.-W., Preston, D., 2010. Interface propagation and microstructure evolution in phase field models of stress-induced martensitic phase transformations. *Int. J. Plast.* 26, 395–422.
- Lookman, T., Shenoy, S.R., Rasmussen, K., Saxena, A., Bishop, A.R., 2003a. Ferroelastic dynamics and strain compatibility. *Phys. Rev. B* 67, 024114.
- Lookman, T., Shenoy, S.R., Rasmussen, K., Saxena, A., Bishop, A.R., 2003b. On dynamics of ferroelastic transitions. *J. Phys. IV: JP* 112, 195–199.
- Rasmussen, K., Lookman, T., Saxena, A., Bishop, A.R., Albers, R.C., Shenoy, S.R., 2001. Three-dimensional elastic compatibility and varieties of twins in martensites. *Phys. Rev. Lett.* 87, 055704.
- Saxena, A., Wu, Y., Lookman, T., Shenoy, S., Bishop, A., 1997. Hierarchical pattern formation in elastic materials. *Phys. A: Statist. Theoret. Phys.* 239 (1–3), 18–34.
- Seol, D., Hu, S., Li, Y., Chen, L., Oh, K., 2002. Computer simulation of martensitic transformation in constrained films. *Mater. Sci. Forum*, 1645–1650.
- Seol, D., Hu, S., Li, Y., Chen, L., Oh, K., 2003. Cubic to tetragonal martensitic transformation in a thin film elastically constrained by a substrate. *Metals Mater. Int.* 9 (3), 221–226.
- Shenoy, S., Lookman, T., Saxena, A., Bishop, A., 1999. Martensitic textures: multiscale consequences of elastic compatibility. *Phys. Rev. B* 60, R12537.
- Theil, F., Levitas, V., 2000. A study of a Hamiltonian model for phase transformations including microkinetic energy. *Math. Mech. Solids* 5 (3), 337–368.
- Truskinovsky, L., 1994a. About the normal growth approximation in the dynamical theory of phase-transitions. *Continuum Mech. Thermodyn.* 6 (3), 185–208.
- Truskinovsky, L., 1994b. Transition to detonation in dynamic phase-changes. *Arch. Rational Mech. Anal.* 125 (4), 375–397.
- Truskinovsky, L., Vainchtein, A., 2006. Quasicontinuum models of dynamic phase transitions. *Continuum Mech. Thermodyn.* 18 (1–2), 1–21.
- Truskinovsky, L., Vainchtein, A., 2008. Dynamics of martensitic phase boundaries: discreteness, dissipation and inertia. *Continuum Mech. Thermodyn.* 20 (2), 97–122.
- Wang, Y., Khachatryan, A., 1997. Three-dimensional field model and computer modeling of martensitic transformations. *Acta Mater.* 45 (2), 759–773.
- WolframResearch, 2007. *Mathematica*. Wolfram Research, Inc., Champaign, Illinois.
- Zienkiewicz, O., Taylor, R., 2000. *The Finite Element Method*. Butterworth-Heinemann, Oxford.